Double-stranded RNA responses, neoantigen presentation and suppression of hepatocellular carcinoma through NMD inhibition via endonuclease SMG6

Enes S. Arpa[1], Virginie Ricci[1], Ilja E. Shapiro[2], Marija Jokic[3], Irene Gonzalez-Menendez[4,5], Leticia Quintanilla-Martinez[4,5], Alexandre P. Bénéchet[6], Jan Rehwinkel[7], Sanjiv A. Luther[3], Michal Bassani-Sternberg[2], David Gatfield[1,8,*]

[1] Center for Integrative Genomics, University of Lausanne, Lausanne, Switzerland.
[2] Ludwig Institute for Cancer Research, University of Lausanne, Lausanne, Switzerland; Department of Oncology, Centre Hospitalier Universitaire Vaudois (CHUV), Lausanne, Switzerland; Agora Cancer Research Centre, 1011 Lausanne, Switzerland.
[3] Department of Immunobiology, University of Lausanne, Epalinges, Switzerland.
[4] Department of Pathology and Neuropathology, University Hospital Tübingen, University of Tübingen, Tübingen, Germany.
[5] Cluster of Excellence iFIT (EXC 2180) "Image-Guided and Functionally Instructed Tumor Therapies", Eberhard-Karls University of Tübingen, Tübingen, Germany.
[6] In Vivo Imaging Facility (IVIF), Department of Research and Training, Lausanne University Hospital and University of Lausanne, Lausanne, Switzerland.
[7] Medical Research Council Translational Immune Discovery Unit, Medical Research Council Weatherall Institute of Molecular Medicine, Radcliffe Department of Medicine, University of Oxford, Oxford, UK.
[8] Lead contact
[*]Correspondence: david.gatfield@unil.ch

SUMMARY

Nonsense-mediated mRNA decay (NMD) eliminates transcripts with premature termination codons, often resulting from mutations or RNA processing errors. While both pro- and anti-tumor NMD activities have been proposed, mechanistic and therapeutic insights into NMD inhibition in cancer have been hindered by the lack of a suitable *in vivo* model. We address this by combining a liver-specific, conditional *Smg6* mutation – disabling the endonuclease that cleaves NMD-regulated transcripts – with a genetic hepatocellular carcinoma (HCC) model. SMG6 inhibition elevates NMD-sensitive mRNA abundance and translation, promotes MHC presentation of unique immunopeptides, and enhances T-cell infiltration. Additionally, mutant SMG6 specifically activates type-I interferon signaling via double-stranded RNA (dsRNA) accumulation and dsRNA-sensor MDA5, boosting innate immune responses. These pathways converge to halt HCC at an inflammatory stage. Our findings establish SMG6 as a key regulator of dsRNA homeostasis and immune activation, offering therapeutic potential and advancing our understanding of NMD in immune regulation.

INTRODUCTION

Eukaryotic gene expression is tightly regulated at the RNA level, with nonsense-mediated mRNA decay (NMD) serving as a critical surveillance pathway. NMD targets and degrades mRNAs harboring premature termination codons (PTCs) [1,2], which can arise from mutations, transcriptional errors or splicing defects [1,2]. If translated, these aberrant mRNAs produce truncated, potentially dysfunctional and harmful proteins. Thus, the traditional view of NMD has been that of an mRNA quality control mechanism that prevents the accumulation of toxic proteins. As such, defining the "rules of NMD" to predict which PTCs elicit or evade degradation has been a major focus of past research [3]. However, NMD extends beyond mere surveillance. It also functions as a broader gene regulatory mechanism, modulating the stability and abundance of a range of physiological transcripts [4]. In both roles, NMD operates in concert with translation termination via a multiprotein machinery centered on the helicase UPF1, eliciting mRNA cleavage through the endonuclease SMG6 further downstream in the pathway, with complete transcript degradation following swiftly through cellular exonucleases.

Cancer cells, with their high mutational burden, frequently display abnormal transcriptomes. For instance, insertions and deletions in protein coding sequences (CDS) often produce frameshifted polypeptides with novel amino acid sequences that have the potential to form neoantigens, i.e., peptides capable of stimulating adaptive immune responses. However, PTCs introduced by these mutations may be targeted by NMD, silencing neoantigen expression and thereby preventing immune responses in cancer. Inhibiting NMD, therefore, represents a potential strategy to restore neoantigen presentation and enhance the efficacy of immunotherapies [3,5-7]. Indeed, experimental models have shown that downregulating NMD components can inhibit tumor proliferation in mice [8-12]. However, these studies – mostly based on inoculation or xenograft models using already fully transformed tumor cells – fail to capture the early stages of oncogenesis and the associated immune dynamics. Moreover, previous approaches that were based on full NMD factor knockouts/depletions could not resolve whether the observed phenotypic outcomes were attributable to the loss of NMD or possibly to confounding effects; notably, UPF and SMG proteins have been associated with NMD-independent functions related to genome stability and telomere maintenance [13]. Taken together, critical questions thus remain unanswered: How does NMD inhibition affect both early and late cancer development in a more physiologically relevant setting? Are neoantigens presented on NMD-deficient cells *in vivo*, even in the absence of cancer? And, importantly, does NMD loss affect other immune pathways, and if so, do they function in a pro- or anti-cancer manner?

70 Here, we address these questions by employing an NMD loss-of-function mouse model,
71 specifically targeting the endonuclease activity of SMG6 and avoiding full knockout, that we
72 combine with a fully immunocompetent genetic model for hepatocellular carcinoma (HCC) that
73 recapitulates cancer development from oncogenic initiation through tumor progression. Our
74 findings reveal how NMD inhibition triggers dual and specific immune responses from both the
75 adaptive and innate systems via distinct molecular mechanisms, effectively blocking HCC
76 development.

77 **RESULTS**

78 **Liver immune cell infiltration in hepatocyte *Smg6^{mut}* animals**

79 We recently developed a conditional NMD loss-of-function mouse model, specifically targeting
80 SMG6 endonucleolytic activity through Cre/loxP-mediated conversion of a wild-type protein-
81 expressing *Smg6^{flox}* allele to *Smg6^{mut}*, where catalytic residues of the PIN (PilT N-terminus)
82 nuclease domain are point-mutated (**Figure 1A**) [14]. This approach overcomes the challenges
83 of full NMD factor knockouts, which typically compromise general cellular fitness, including
84 through mechanisms that rely on functions of these proteins distinct from NMD [13,15]. Liver-
85 specific *Smg6^{mut}* mice (i.e., *Smg6$^{flox/flox}$*; *Alb^{CreERT2}* animals, treated with tamoxifen for Cre
86 activation in hepatocytes) show overall mild phenotypes [14], highlighting the model's suitability
87 for therapeutic exploration. Further analyses of our previous liver transcriptomics datasets [14]
88 revealed elevated expression of several leukocyte marker genes in *Smg6^{mut}* tissue,
89 suggesting immune cell infiltration when SMG6 endonucleolytic activity was disabled in
90 hepatocytes (**Figure S1A**). To validate this hypothesis, we carried out flow cytometric analysis
91 to count immune cells from livers collected at an early timepoint (3 weeks) after tamoxifen
92 treatment (**Figure 1B**). Indeed, total leukocyte counts were increased in *Smg6^{mut}* vs. matched
93 control *Smg6^{wt}* livers (**Figures 1C**, **S1B,** and **S1C**), with key adaptive and innate immune cell
94 types – such as activated T-cells, dendritic cells and monocytes (**Figure 1D**) – contributing to
95 the overall effect. Together with indications that several liver damage markers in serum were
96 above wild-type levels (**Figure S2A**) and that markers of inflammation (**Figure S2B**) and
97 apoptosis (**Figures S2C** and **S2D**) were significantly increased as well, we concluded that the
98 *Smg6* mutation had the ability to induce an immune-altered liver and led to increased
99 hepatocyte turnover.

100 **Noncanonical immunopeptide expression from NMD substrates**

101 Key adaptive immune cell types, such as activated T-cells (**Figure 1D**), contributed to the
102 immune-altered state, possibly induced by neoantigens. Employing a multi-omics approach
103 that combined transcriptomics (RNA-seq), ribosome profiling (Ribo-seq), and
104 immunopeptidomics (**Fig. 1E**), we explored whether novel major histocompability complex

105 class-I (MHC-I) polypeptides could be specifically detected in *Smg6*^{mut} livers and if these
106 peptides originated from the translation of transcripts regulated by NMD. Immunopeptidomics
107 analyses revealed over 2,000 MHC-I binders (**Figure 1F**; **Table S1**), with most peptides
108 shared between *Smg6*^{mut} and *Smg6*^{wt} livers (**Figure 1F**). As expected, these primarily mapped
109 to canonical coding sequences (**Figure 1G**, left panel). In contrast, 18 peptides were identified
110 exclusively in *Smg6*^{mut} samples (present in all replicates) and were absent in *Smg6*^{wt},
111 compared to only 4 peptides with the reverse pattern (**Figure 1F**) – a highly significant
112 enrichment of novel peptides associated with NMD deficiency (P = 5.4e-05; Fisher's exact
113 test). Notably, among the *Smg6*^{mut}-specific peptides, three were derived from noncanonical
114 coding sequences annotated as exonic and one as intronic (**Figure 1G**, middle and right
115 panels), all of which were abundant in the three *Smg6*^{mut} replicates and absent in controls
116 (**Figure 1H**). Further validation in the Ribo-seq and RNA-seq data for one of the peptides,
117 SAPDGIKTPM, indicated that it mapped to the *D17H6S56E-5* gene, a lncRNA-annotated
118 locus with previously reported resemblance to a Mouse Leukemia Virus (MLV) envelope
119 protein coding gene [16]. The RNA-seq data revealed increased abundance of the *D17H6S56E-*
120 *5* transcript in *Smg6*^{mut} livers (**Figures 1I** and **1J**), which was striking for exon-mapping reads,
121 yet less pronounced for reads mapping to an intron that the gene contains. Intron-mapping
122 reads can be used as a proxy for transcription from the locus [17], and these findings hence
123 indicate that *D17H6S56E-5* upregulation occurs mainly through posttranscriptional
124 mechanisms (i.e., mRNA stabilization), in line with the mRNA being an NMD substrate. The
125 Ribo-seq data further confirmed efficient translation of a 596 amino acid (aa) open reading
126 frame (ORF) containing the immunopeptide towards its N-terminus (**Figure 1J**). For the
127 VVITFSKM peptide (**Figure 1H**), we could similarly determine a relevant locus,
128 *Gm6545*/*A330040F15Rik*, containing a pseudogene copy of *Fam111a* that is upregulated at
129 the level of RNA abundance and ribosome footprint coverage on a 554 aa ORF (**Figure S2E**),
130 whereas the two other peptides, VSTTNFTHA and AGPSNSEIHL, mapped to an out-of-frame
131 translation product from the *Hfe2* locus and an intronic sequence of *Trf*, respectively (**Table**
132 **S1**). We concluded that *Smg6* mutation led to the expression of non-canonical transcripts that
133 became translated to proteins that were the source of novel MHC-I-loaded immunopeptides,
134 in line with the observed infiltration by activated CD8+ T-cells.

135 **SMG6-dependent, cell-autonomous type-I IFN response**

136 We next investigated whether the recruitment of innate immune cells was triggered by a
137 specific, *Smg6*-dependent mechanism as well. This hypothesis was supported by the
138 *Smg6*^{mut}-dependent increase in expression of NF-κB-regulated inflammatory response genes
139 (see **Figure S2B**) and RNA-seq data showing upregulation of a broad panel of transcripts [18]
140 indicative of an activated type-I interferon (IFN) response (**Figure 2A**). Quantitative real-time

141 PCR (qPCR) analysis of key IFN-stimulated genes (ISGs), *Ifih1*, *Oas1a*, *Ifi44*, *Zbp1*, and *Ifit1*,
142 confirmed robust *Smg6*^{mut}-dependent upregulation (**Figure 2B**), consistent with sustained
143 type-I IFN pathway activation. In the context of the full liver tissue – consisting of *Smg6*^{mut}
144 hepatocytes and other cell types including infiltrating leukocytes that were *Smg6*^{wt} – ISG
145 induction could be dependent on hepatocyte-immune cell interactions, or it could represent a
146 cell-autonomous consequence of mutant SMG6. To test this, we used an *ex vivo* model with
147 *Smg6*$^{flox/flox}$ primary fibroblasts retrovirally engineered to express a tamoxifen-activatable
148 CreERT2 (**Figure 2C**) [14]. Tamoxifen treatment induced a >10-fold increase in abundance of
149 an NMD-sensitive *Hnrnpl* splice variant, confirming NMD pathway inactivation (**Figure 2D**).
150 Importantly, NMD inactivation led to a massive induction (up to several hundredfold) of ISGs,
151 *Ifih1*, *Oas1a*, *Ifi44*, *Zbp1*, and *Ifit1* (**Figure 2E**), demonstrating that SMG6 mutation directly
152 triggers a type-I IFN response in a cell-autonomous manner.

153 **Requirement of dsRNA sensor MDA5 for SMG6-dependent IFN response**

154 The type-I IFN response is a key antiviral defense mechanism, activated when cytoplasmic
155 sensors detect atypical nucleic acids, including double-stranded RNA (dsRNA). Besides viral
156 infections, endogenous dsRNA can also arise through non-viral mechanisms and enhance
157 anti-tumor immunity and/or cancer cell apoptosis. For instance, anti-tumor strategies that
158 inhibit splicing lead to the leakage of intron-containing mRNAs into the cytoplasm, where they
159 form dsRNA structures likely due to repetitive element sequences within introns [19-21].
160 Activation of the dsRNA sensor MDA5, encoded by the *Ifih1* gene, triggers a type-I interferon
161 (IFN) response similar to that in antiviral defense [21]. In our hepatocyte *Smg6* mutant model,
162 transcripts containing retained introns accumulate as major mRNA species that fail to undergo
163 NMD [14], prompting us to investigate whether the ISG induction observed in our model also
164 involved the dsRNA-MDA5 pathway. To this end, we generated *Smg6*$^{flox/flox}$ fibroblast lines
165 with an inactivated *Ifih1* gene (**Figures 2F**, **S3A,** and **S3B**) and induced Cre-mediated
166 recombination of *Smg6*^{flox} to *Smg6*^{mut} by delivering cell-permeable recombinant TAT-Cre
167 protein (**Figure 2G**). NMD inhibition, measured via the diagnostic *Hnrnpl* splice form, remained
168 intact in MDA5-deficient cells (**Figure 2H**). Importantly, however, the marked increase in ISG
169 expression observed in the presence of MDA5, was significantly blunted in *Ifih1* knockouts,
170 now remaining close to background (**Figure 2I**). Moreover, consistent with the hypothesis that
171 *Smg6*^{mut} leads to cytoplasmic dsRNA accumulation, immunostaining with the dsRNA-specific
172 J2 antibody [22] showed elevated signal in *Smg6*^{mut} fibroblasts compared to control (**Figures 2J**
173 and **2K**). These findings suggest that the molecular pathway linking endonuclease-inactive
174 SMG6 and the type-I IFN response relies on the dsRNA sensor MDA5. Notably, the specificity
175 of these phenotypes for *Smg6*^{mut} and MDA5 also rules out potential non-specific effects

176 associated with Cre recombinase activity, which have been reported to act via DNA damage
177 and the independent cGAS-STING sensing pathway [23].

178 **SMG6-dependent amplification of early inflammation in a hepatocellular carcinoma**
179 **model**

180 To investigate how SMG6-dependent adaptive and innate immune activation influences early
181 and late stages of tumor development, we combined our NMD allele with a hepatocellular
182 carcinoma (HCC) model. This model (**Figure 3A**) employs conditional alleles of two tumor
183 suppressors, *Pten* and *Tsc1*, encoding inhibitors of the mTOR pathway. Liver-specific
184 knockout of these genes promotes lipogenesis, leading to non-alcoholic fatty liver disease
185 (NAFLD) and non-alcoholic steatohepatitis (NASH), ultimately progressing to HCC [24], closely
186 resembling human disease [25]. In animals carrying the cancer alleles (*Pten*$^{flox/lfox}$; *Tsc1*$^{flox/flox}$;
187 *Alb*^{CreERT2} – termed "Liver double knockout" or "L-dKO") along with either *Smg6*$^{flox/flox}$ or
188 *Smg6*$^{wt/wt}$, we first examined early stages (3 weeks post-tamoxifen, **Figure 3B**). Western blot
189 analysis confirmed significantly reduced TSC1 and PTEN protein levels in L-dKO livers,
190 independent of *Smg6* allele (**Figure 3C** and **3D**). Macroscopically and histologically, both L-
191 dKO *Smg6*^{wt} and *Smg6*^{mut} livers displayed NASH features, with focal microsteatosis, abnormal
192 cytoskeleton (ballooning), increased inflammatory infiltrate and necrosis (**Figures 3E** and
193 **S4A**). Notably, the presence of inflammatory infiltrate was more pronounced in L-dKO *Smg6*^{mut}
194 livers, supported by staining for the neutrophil/monocyte marker Myeloperoxidase (MPO)
195 (**Figure 3F**, left panels) and the T-cell marker CD8 (**Figures 3F**, right panels, **3G**). Hepatic
196 leukocyte quantification via flow cytometry-based counting revealed elevated infiltration
197 (**Figure 3H**), and among innate immune cells, both subsets of monocytes (Ly6c^{high} and
198 Ly6c^{low}) and neutrophils were particularly increased in L-dKO *Smg6*^{mut} livers compared to L-
199 dKO *Smg6*^{wt} livers (**Figures 3H** and **3I**) or compared to *Smg6*^{mut} livers without the L-dKO
200 background (**Figures 1C** and **1D**). Additional observations supported this synergistic effect on
201 immune responses in the presence of both L-dKO alleles and mutant SMG6. Notably,
202 apoptotic markers indicated increased cell death (**Figures S4B-F**), pro-fibrotic gene
203 expression suggested increased liver damage (**Figure S4G**), hepatomegaly was prominent
204 (**Figure S5A**), and serum damage markers were elevated (**Figure S5B**). These findings reveal
205 that NMD inhibition in L-dKO strongly amplified early inflammation, lymphocyte infiltration, and
206 apoptosis during the NAFLD/NASH stage i.e., at a timepoint before tumor development in this
207 HCC model.

208 **HCC suppression through mutant SMG6**

209 We next assessed the impact of *Smg6*^{mut} on the formation and progression of HCC at late-
210 stage (**Figure 3B**). Weekly magnetic-resonance imaging (MRI) showed tumors in the livers of

211 L-dKO *Smg6*^{wt} mice starting at week 12 (**Figure 4A**), with rapid progression that required
212 sacrifice latest by week 17 due to advanced-stage HCC (**Figure 4B**). Crucially, L-dKO *Smg6*^{mut}
213 mice did not develop any tumors and none of the animals required sacrifice, indicating full
214 suppression of the HCC phenotype. Macroscopic and histological analyses confirmed HCC in
215 L-dKO *Smg6*^{wt} (**Figure 4C**, top). Instead, from week 12 and until the experimental endpoint at
216 week 21, L-dKO *Smg6*^{mut} mice presented with prominent duct proliferation and moderate
217 perisinusoidal and periportal fibrosis, altering the hepatic parenchyma structure and leading
218 to a nodular architecture (**Figure 4C**, bottom). CD8+ T-cell levels remained elevated in late-
219 stage L-dKO *Smg6*^{mut} livers (**Figures 4D** and **4E**), suggesting continued augmented adaptive
220 immune responses. By contrast, some other liver parameters showed tendencies to
221 stabilization. In particular, liver damage markers in serum showed recovery as compared to
222 early-stage livers (**Figure S5A**) and hepatomegaly between early- and late-stage L-dKO
223 *Smg6*^{mut} only showed mild further increase (non-significant; **Figure S5B**). Importantly, L-dKO
224 *Smg6*^{mut} livers still displayed expression of the recombined, mutant *Smg6* mRNA (**Figure S5C**)
225 as well as the absence of PTEN and TSC1 proteins from hepatocytes (**Figures S5D** and **S5E**),
226 with remaining protein localizing to non-hepatocyte cells such as Kupffer cells (**Figure S5F**).
227 These findings controlled for potentially trivial explanations to the absence of HCC – such as
228 lethality of the allele combination *Smg6*^{mut}; *Pten*^{ko}; *Tsc1*^{ko} and regeneration of non-mutant
229 tissue – and demonstrated that the suppression of tumor formation was the result of the
230 specific interaction of mutant SMG6 with the tumor-prone, *Pten*- and *Tsc1*-deleted genetic
231 state. In summary, we concluded that the inhibition of NMD via *Smg6* mutation prevents
232 cancer formation in the genetic HCC model.

233 **DISCUSSION**

234 We demonstrate that targeting the endonuclease function of SMG6 to inhibit NMD shows
235 therapeutic benefits as it prevents tumor formation in a fully immunocompetent HCC model,
236 leading instead to NASH. Mechanistically, our data are consistent with a simple model in which
237 both innate and adaptive immune responses are triggered as a direct consequence of
238 stabilized SMG6 target transcripts, involving two distinct downstream mechanisms (**Figure**
239 **4F**). Consistent with the long-postulated neoantigen hypothesis, we provide evidence for
240 NMD-specific, endogenous MHC-I peptides originating from non-canonical protein coding
241 sequences that could be presented to CD8+ T-cells.
242 Importantly, we identify a new mechanism for the innate immune activation via the dsRNA
243 sensor MDA5 that triggers an antiviral-like type-I IFN response – a step that in the logic of
244 immune activation would precede and stimulate the subsequent adaptive response. This
245 SMG6-dependent response may involve intron-retained transcripts that fold into dsRNAs due
246 to the enrichment for repetitive elements in intronic sequences – analogous to the pathway

247 and mechanism associated with anticancer spliceosome inhibition [19,20]. Intriguingly, our
248 findings hence also suggest a novel biological function of the NMD pathway in the control of
249 immune responses, which would directly implicate the NMD-targeted RNAs, rather than the
250 proteins that are translated from these erroneous, PTC-containing transcripts. Under wild-type
251 conditions, we propose that NMD/SMG6 reduces cytoplasmic dsRNAs, thus setting the
252 threshold to prevent overactivation of the type-I IFN response – a likely crucial, yet so-far
253 underappreciated, immune regulatory role of NMD.
254 Our *in vivo* findings indicate that NMD serves as a protective barrier for cancer cells, limiting
255 neoantigen expression and immune activation. Therapeutic targeting of SMG6 – whose
256 mutation is well-tolerated in our model – emerges as a promising avenue for anticancer
257 treatment. Development of a pharmacological SMG6 endonuclease inhibitor could allow for
258 the precise modulation of immune activation against HCC, balancing effective immune
259 responses while minimizing the risk of fibrosis and autoimmune complications.

260 **STAR★METHODS**

261 **Animals**

262 All animal experiments were conducted in accordance with the cantonal guidelines of the
263 Canton of Vaud, Switzerland, license VD3739. Healthy adult male mice of age 8 to 10 weeks
264 were used. Animals with *Alb*^{CreERT2}; *Smg6*^{wt} and *Alb*^{CreERT2}; *Smg6*^{flox} alleles were maintained
265 on a C57BL/6J background. Mice with *Alb*^{CreERT2}; *Pten*^{flox}; *Smg6*^{wt}; *Tsc1*^{flox} and *Alb*^{CreERT2};
266 *Pten*^{flox}; *Smg6*^{flox}; *Tsc1*^{flox} alleles were maintained on a hybrid background (C57BL/6J, 129SvJ,
267 and BALB/2c). The alleles *Alb*^{CreERT2}, *Pten*^{flox}, *Smg6*^{flox}, and *Tsc1*^{flox} have been previously
268 described [14,26-28].

269 **Induction of hepatocyte-specific *Pten* & *Tsc1* double knockout and *Smg6* mutation**

270 8- to 10-week-old male L-dKO *Smg6*^{wt} and *Smg6*^{flox} mice, carrying the liver-specific *Albumin*-
271 driven *CreERT2*, and their control littermates received four intraperitoneal injections of
272 tamoxifen, dissolved in corn oil at a dosage of 75 mg/kg of body weight, in the consecutive
273 days. The early-stage mice were euthanized 3 weeks after tamoxifen injections. In the late-
274 stage experiment, L-dKO *Smg6*^{wt} mice were euthanized based on the progression of HCC
275 (latest at week 17). Animals in the other groups (Ctrl *Smg6*^{wt}, Ctrl *Smg6*^{mut} and L-dKO *Smg6*^{mut})
276 were euthanized 21 weeks after tamoxifen injections.

277 **Magnetic resonance imaging (MRI)**

278 Mice were scanned weekly (starting from week 12), to monitor HCC evolution and progression,
279 using a 3 Tesla small animal MRI scanner (Bruker BioSpin MRI, Ettlingen, Germany) with a
280 40-mm volume coil as a transmitter. Animals were anaesthetized using isoflurane (Attane) at
281 3-4% for 2 min. When fully sedated, animals were transferred into the MRI machine. The
282 imaging procedure was performed under 1.5% isoflurane in oxygen. Data was acquired via
283 Paravision 360 v2.0 software.

284 **Histopathology and immunohistochemistry analyses**

285 Livers were fixed in 4% buffered formalin for 24 h and embedded in paraffin. For histology 3-
286 5 µm-thick sections were cut and stained with Hematoxylin and Eosin (H&E) and Masson's
287 Trichrome (MTC). Immunohistochemistry was performed on an automated immunostainer
288 (Ventana Medical Systems, Inc.) according to the company's protocols for open procedures
289 with slight modifications. All slides were stained with the antibodies CD4 (SP35; Zytomed,
290 Berlin, Germany), CD8 (C8/144B; Dako, Glostrup, Denmark), PTEN (Cell Signaling
291 Technology, 9188), Cleaved-Caspase3 (Cell Signaling Technology, 9661), and MPO (anti-
292 MPO Ab-1, Lab Vision UK, Ltd., Newmarket, Suffolk, Great Britain). Appropriate positive and
293 negative controls were used to confirm the adequacy of the staining. The histologic samples

294 were analyzed by an experienced pathologist (L. Quintanilla-Martinez). All samples were
295 scanned with the Ventana DP200 (Roche, Basel, Switzerland) and processed with the Image
296 Viewer MFC Application. Final image preparation was performed with Adobe Photoshop 2024.

297 **Intrahepatic leukocyte isolation and flow cytometry staining**

298 Leukocytes in liver were isolated as described previously [29]. Mice were euthanized and
299 subsequently perfused with 10 ml 1x PBS via the inferior vena cava. 1 g of liver tissue was
300 excised from each mouse and placed into a tube containing 10 ml RPMI. The tissues were
301 then crushed using 70 µm cell strainers and a plunger, ensuring all pieces were passed
302 through the strainer. The resulting cell suspensions were centrifuged at 1600 x g for 5 min.
303 The cell pellets were resuspended in a solution containing 2 mg collagenase, 25 µl DNase
304 and 10 ml RPMI. The mixture was incubated at 37°C for 40 min, constantly stirring. After
305 incubation, 25 ml RPMI was added to dilute the mixture. The samples were then centrifuged
306 at 300 x g for 3 min to precipitate the connective tissue. The supernatants were transferred to
307 new tubes and centrifuged at 1600 x g for 5 min. The cell pellets were then resuspended in a
308 Percoll density gradient solution (36% Percoll [Cytiva], 4% 10x PBS, 60% RPMI) and
309 centrifuged at 2000 x g for 20 min without brake. The pellets were resuspended with 2 ml of
310 Ammonium-Chloride-Potassium (ACK) lysis buffer for 2 min to lyse remaining red blood cells.
311 Following that, 8 ml RPMI was added to the tubes, and the samples were centrifuged at 1600
312 x g for 5 min. The purified leukocyte pellets were resuspended in 1 ml HBSS. The cells were
313 blocked with anti-CD16/32, and then washed with flow cytometry buffer (1x PBS, 2% FCS,
314 2mM EDTA). Next, the cells were incubated with following primary antibodies for 25 min at
315 4°C in the dark: CD19-BV605 (BD biosciences, 563148), TCRb-PE (BD biosciences, 12-5961-
316 81), CD4-biotin (homemade), CD8a (Biolegend, 100750), CD44-FITC (homemade), CD11b-
317 FITC (Biolegend, 101206), CD45-PE-Cy7 (Biolegend, 10114), Ly6c-BV785 (Biolegend,
318 128041), Ly6G-APC-Cy7 (Biolegend, 127624), CD19-PE (Immunotools, 22190194), TCRb-
319 PE (BD biosciences, 12-5961-81), MHCII-BV711 (Biolegend, 107643), CD11c-biotin
320 (homemade), NK1.1 (BV605, 108753), Streptavidin (APC, 405207) and BV510-Zombie aqua
321 (Biolegend, 423102). Following washes with flow cytometry buffer, the cells were incubated
322 with secondary antibodies for 20 min at 4°C in the dark. The cells were fixed with BD fixation
323 kit (554714).

324 **Serum parameters**

325 Following the euthanasia of the animals, blood was quickly collected from the decapitated
326 body, and then transferred into a lithium-heparin (LiHep) added tube (BD microtainer) to obtain
327 serum. After 30 min to 1 h incubation at room temperature (RT), samples were centrifuged

328 (2,000 g x 10 min, RT) to separate serum. Following that, 100 µl of serum was loaded to a
329 Cobas c111 analyzer to measure the levels of following enzymes: ALT, AST and LDH.

330 ***Smg6* cDNA genotyping**

331 Total RNA was prepared as described previously [30]. For each RNA sample, the following
332 reaction was assembled: 4.5 µg RNA, 1.5 µl random hexamer (100 µg/ml), 1.5 µl 10 mM
333 dNTPs, RNase-free water to 18 µl. Samples were heated for 5 min at 65°C, and then
334 immediately put on ice. A master mix containing the following was added to each tube: 6 µl 5x
335 First-strand buffer, 3 µl 0.1 M DTT, 0.375 µl RNase inhibitor, 1.5 µl RNase-free water. After a
336 short incubation (2 min, at RT), 1.125 µl Superscript II reverse transcriptase enzyme was
337 added to each reaction. Samples were incubated 10 min at 25°C, 50 min at 42°C, 15 min at
338 70°C, respectively. *Smg6* genotyping polymerase chain reaction (PCR) was performed as
339 described previously [14]. The primer sequences – encompassing both mutant sites – are as
340 follows: forward: CCA GAT ACC AAC GGC TTC AT; reverse: TCT GGG TGG ATT GGT AGC
341 TC. Reactions were run on a 0.8% agarose gel, at 100 V for 100 minutes. Bands
342 corresponding to ~620 nt were excised, and then purified using Qiaquick Gel Extraction Kit
343 (QIAGEN, 28704). DNAs were Sanger-sequenced by Microsynth.

344 **Quantitative Reverse Transcriptase PCR**

345 Total RNA was prepared, and cDNA was synthesized as mentioned above. 10-times diluted
346 cDNA templates and a master mix containing SYBR green master mix (2x), forward and
347 reverse primers (3.0 µM) were mixed, and then a 384-well plate was prepared using the Tecan
348 Freedom EVO software. RT-PCR was performed using QuantStudio6 real-time systems.
349 Relative mRNA expression levels were obtained by normalizing each CT value (mean of three
350 technical replicates) to *Rpl13* and *Rpl27* expressions. The qPCR primer sequences can be
351 found in Supplementary Table 2.

352 **Transcriptomics analysis**

353 Total RNA was prepared as mentioned above. RNA-seq libraries were prepared from
354 individual mouse livers according to the standard protocols. Single-end sequencing (150
355 bases) was performed on NovaSeq6000 (Illumina) with a sequencing depth of 400 million
356 cDNA-mapping reads in total. Sequencing reads were trimmed for the first two low quality
357 (nucleotides) nt. Trimmed reads were then mapped using STAR [31] (v2.7.11b; --twopassMode
358 Basic --seedSearchStartLmax 50 --outSAMmultNmax 1) in a sequential manner: mouse rRNA
359 (Ensembl version 39.111), human rRNA (Ensembl version 38.111), mouse tRNA, and mouse
360 genome. Read counts per genes were obtained using summarizeOverlaps() of the R (v4.4.0)
361 library GenomicAlignments (mode = 'Union') and low read counts were excluded (≤5 counts

362 in less than three samples). Differential gene expression analysis was performed using
363 DEseq2 [32].

364 **Ribosome profiling**

365 The libraries for ribosome profiling were generated as [33] with slight changes. Frozen liver
366 tissues (200 mg) from individual mice were homogenized with 5 strokes using a Teflon
367 homogenizer in 3 volumes of polysome buffer (150 mM NaCl, 20 mM Tris-HCl [pH 7.4], 5 mM
368 DTT, complete EDTA-free protease inhibitors [Roche] and 40 U/ml RNasin plus [Promega])
369 supplemented with 1% Triton X-100 and 0.5% Na deoxycholate. Liver lysates were incubated
370 on ice for 10 min and cleared by centrifugation at 10,000 g, 4°C for 10 min. Supernatants were
371 flash-frozen and stored in liquid nitrogen. For each sample, 15 OD_{260} of liver lysate was
372 digested with RNase I (Ambion) for 45 min at RT under constant shaking. RNase I-digested
373 RNA was separated on 15% urea-polyacrylamide gels to excise monosome (~30 nt) footprints.
374 From the gel slices, RNA was extracted overnight at 4°C on a rotating wheel before
375 precipitation in isopropanol for 1 h, at -20°C. RNA 3'-end repair was performed with 2 U/µl of
376 T4 PNK (Lucigen) before 2 h of adapter ligation at 25°C using T4 RNA Ligase 1 (NEB) and
377 T4 RNA Ligase 2 Deletion Mutant (Lucigen) and 1 µl of a 20 µM 5'-adenylated DNA adapter.
378 Adapter removal was performed by treating individual libraries with 5'deadenylase (NEB) and
379 RecJf exonuclease (NEB) for 1 h at 30°C and 1 h at 37°C. Samples were purified and pooled
380 using Zymo Clean & Concentrator columns. Ribosomal RNA was depleted according to
381 siTools Biotech rRNA depletion kit specifications with a custom-made riboPOOL. The clean-
382 up step was performed using Zymo Clean & Concentrator columns. Further library preparation
383 steps were performed as described. The amplification of libraries was performed using i5 and
384 i7 [NexteraD502 or NexteraD503] primers. Libraries were sequenced on a NovaSeq6000
385 (Illumina).

386 **Ribosome profiling data analysis**

387 Sequencing reads were cleaned and trimmed. Briefly, adapter sequences were removed
388 using cutadapt (v3.5) [34] with the following parameters --match-read-wildcards --overlap 8 --
389 discard-untrimmed --minimum-length 30. Reads were filtered by quality using FASTX Toolkit
390 (v0.0.14; -Q33 -q 30 -p 90) and by size using an in-house Python script (length 26-35 nt).
391 Cleaned reads were then mapped using STAR (--twopassMode Basic –seedSearchStartLmax
392 28 –outSAMmultNmax 1) [31] in a sequential manner: mouse rRNA (Ensembl version 39.111),
393 human rRNA (Ensembl version 38.111), mouse tRNA, and mouse genome. STAR was used
394 for the mapping to splice junctions, as neoantigens can be produced from both exons and
395 introns. The A-site position of mapped reads to the mouse genome was retrieved using the R
396 (v4.4.0) package ribosomeProfilingQC (v1.16.0; estimatePsite() and getPsiteCoordinate(),

397 and addition of 3 nt to recover the A-site position). The A-sites were assigned to the counting
398 bins and the A-site count per bin was retrieved. Counting bins were defined using an in-house
399 R script (main functions: makeTxDbFromGFF() from txdbmaker [v1.1.1]; exonicParts() from
400 GenomicFeatures [v1.57.0]; and reduce(), gaps(), and findOverlaps() from IRanges [v2.39.2])
401 and A-site counts were obtained using summarizeOverlaps() of GenomicAlignments (v1.41.0;
402 mode = 'Union') [35]. The low A-site counts (≤5 counts in less than three samples) were excluded
403 and the differential analysis was performed using DESeq2 (v.1.45.3). To identify putative
404 neoantigens, the median A-site counts were calculated for each condition and the bins with at
405 least one A-site count in L-dKO *Smg6*^{mut} were retained. The nucleotide sequences of each bin
406 were extracted, translated in the three reading frames, and the resulting amino acid sequences
407 were then split by stop codon, and retained if the peptide sequence lengths were ≥ 8 amino
408 acids.

409 **MHC-I antibody production**

410 MHC-I monoclonal antibodies were purified from the supernatant of HB-51 and HIB 34.1.2
411 hybridoma cells (ATCC), respectively, with Protein A-Sepharose 4B beads (Invitrogen). HB-
412 51 has specificity for H2-Db and H2-Kb, HIB 34.1.2 has specificity for H2-Dd, H2-Kd, and H2-
413 Ld. Each antibody type was cross-linked separately to Protein A-Sepharose 4B beads at
414 concentrations of 5 mg of antibodies per 1 ml of bead volume. To this end, the antibodies were
415 incubated with Protein A-Sepharose 4B beads for 1 hour, at RT. Antibodies and beads were
416 cross-linked with dimethyl pimelimidate dihydrochloride (Sigma-Aldrich) in 0.2 M sodium
417 borate buffer pH 9 (Sigma-Aldrich) to achieve a final concentration of 20 mM for 30 min. The
418 reaction was quenched via incubation with 0.2 M ethanolamine pH 8 (Sigma-Aldrich) for 2
419 hours. Cross-linked antibodies were stored at 4°C.

420 **Purification of MHC-I-eluted peptides**

421 200 mg of liver tissue per biological replicate was lysed in 2 ml phosphate buffered saline with
422 0.5% sodium deoxycholate (Sigma-Aldrich), 0.2 mM iodoacetamide (Sigma-Aldrich), 1 mM
423 EDTA, 1:200 Protease Inhibitor Cocktail (Sigma-Aldrich), 1 mM phenylmethylsulfonylfluoride
424 (Roche), and 1% octyl-beta-D glucopyranoside (Sigma-Aldrich) at 4°C for 1 hour, after
425 homogenization with an IKA T10 standard ULTRA TURRAX. Lysates were cleared by
426 centrifugation with a table-top centrifuge (Eppendorf Centrifuge) at 4°C at 20,000 g for 50 min.
427 MHC-I molecules purification was done with HB51 antibodies for C57BL/6 and a 1:1 mix of
428 HB51, HiB antibodies for C57BL/6; BALB/2c; 129_SvJae. Immunoprecipitations in 96-well
429 plates followed the protocol of [36]. Shortly, after plate conditioning, cross-linked beads and then
430 lysates were added to single wells, followed by washes at different sodium chloride
431 concentrations and an acidic elution step. Peptides were then desalted and purified on C18-

432 columns. Recovered peptides were dried using vacuum centrifugation (Thermo Fisher
433 Scientific) and stored at -80°C.

434 **Mass-spectrometry acquisition**

435 For Mass spectrometry (MS) analysis, MHC-I peptide samples were resuspended in 8 µl of
436 2% ACN and 0.1% formic acid (FA). 3 µl of peptide resuspension was injected into the LC-MS
437 setup per measurement, counting two in DDA and one in DIA. The LC-MS setup consists of
438 an Easy-nLC 1200 (Thermo Fisher Scientific) connected to a Q Exactive HF-X (Thermo Fisher
439 Scientific). Chromatographic separation was done with a 450 mm homemade column of 75
440 µm inner diameter packed with ReproSil Pur C18-AQ 1.9µm resin (Dr. Maisch GmbH). For
441 DDA measurements, the chromatographic separation was performed over 2 hours using a
442 gradient of H_2O:FA, 99.9%:0.1% (solvent A) and CH_3CN:FA 80%:0.1% (solvent B). The
443 gradient consisted of sequential, linear steps: 0 to 110 min (2-25% B), 110 to 114 min (25-
444 35% B), 114 to 115 min (35-100% B), and 115 to 120 min (constant at 100% B) at a flow rate
445 of 250 nl/min. The mass spectrometer had the following parameters set: full-scan MS spectra
446 were acquired from m/z = 300-1,650 at a resolution of 60,000 (m/z = 200) with maximum
447 injection times of 80 ms. Auto gain control (AGC) target value was tuned to 3 x 10^6 ions. We
448 acquired MS/MS spectra at a resolution of 30,000 (m/z = 200), a top 20 method and isolation
449 windows of 1.2 m/z, as well as a collision energy of 27 (HCD). All MS/MS scans accumulated
450 ions to an AGC target value of 2 x 10^5 at a maximum injection time of 120 ms. Precursors of
451 charge 4 and above were not selected for fragmentation. The dynamic exclusion was set to
452 20s. For DIA, the chromatographic separation was performed as in DDA measurements. The
453 DIA acquisition cycles included one full-scan MS spectra, acquired from m/z = 300-1,650
454 (Resolution = 120,000, ion accumulation time = 60 ms), and 22 MS/MS scans. For all MS/MS
455 scans the AGC target value was set to 3 x 10^6 ion, mass resolution at 30,000 and a stepped
456 normalized collision energy (25.5, 27, 30) was applied. The maximum ion accumulation was
457 set to auto and their first mass was fixed to 200 m/z. Consecutive MS/MS scans overlapped
458 in their m/z windows by 1 m/z.

459 **Immunopeptidomics data processing**

460 All DDA files were used to generate a library with a database search using FragPipe (v22.0),
461 including MSFragger (v4.1) [37]. The FASTA file was compiled as described in 'Ribosome
462 profiling data analysis'. For search space generation, unspecific digestion with peptide lengths
463 of 8 to 14 amino acids was used. Variable modifications included methionine oxidation, N-
464 terminal acetylation, and cysteine carbamidomethylation. No fixed modifications were applied.
465 Peptide, ion, and psm FDRs were set to 0.03 while applying a group-specific FDR as indicated
466 in the FASTA header with PE = X, X being the respective protein group. No protein FDR was

467 applied. All other settings were set to default. DIA files were searched with the library
468 described above using DIA-NN (v1.8) with a precursor q-value cut-off of 0.01. Peptide binding
469 affinities were predicted with MixMHC [38]. Peptides were considered as binders when they had
470 a %-rank below 2 for at least one HLA allele present in the sample haplotypes. Data analyses
471 were done with Julia and R, visualizations with R.

472 **Protein extraction and Western Blot**

473 Total proteins from mouse liver samples were isolated according to the NUN (NaCl, Urea,
474 Nonidet P-40) procedure, as [14]: Livers were homogenized in two tissue volumes of 10 mM
475 Hepes (pH 7.6), 100 mM KCl, 0.1 mM EDTA, 10% glycerol, 0.15 mM spermine, and 0.5 mM
476 spermidine for 15 s using a Teflon homogenizer. Four tissue volumes of 2x NUN buffer (2 M
477 urea, 2% NP-40, 0.6 M NaCl, 50 mM Hepes [pH 7.6], 2 mM dithiothreitol, and 0.1 mM
478 phenylmethylsulfonyl fluoride; supplemented with complete protease inhibitor tablets, Roche)
479 were added dropwise on a vortex with low speed. Lysates were incubated 1 h on ice and
480 cleared through centrifugation at 10,000 rpm, 4°C, for 20 min. Aliquots of the lysates (40 µg
481 of protein loaded per lane) were separated by SDS-polyacrylamide gel electrophoresis and
482 transferred to PVDF membrane using an iBlot 2 gel transfer device. The membrane was
483 blocked using 5% milk in Tris-buffered saline with 0,1% Tween 20 (TBST), 1 h at RT, followed
484 by an incubation overnight at 4°C with appropriate dilutions of primary antibodies, including
485 anti-Cleaved CASPASE3 (Cell Signaling Technology, 9661), anti-MDA5 (Cell Signaling
486 Technology, 5321), anti-PTEN (Cell Signaling Technology, 9188), anti-Hamartin/TSC1 (Cell
487 Signaling Technology, 6935), anti-GAPDH (Cell Signaling Technology, 2118), and anti-
488 VINCULIN (Abcam, ab129002). Following TBST washing (5 min, three times), the membrane
489 was incubated with the appropriate secondary antibody conjugated with horseradish
490 peroxidase for 60 min at RT, followed by TBST washing (15 min, three times).
491 Chemiluminescence signal was detected using Supersignal West Femto Maximum Sensitivity
492 Substrate (Thermofisher Scientific, 34095), as described by the manufacturer. The
493 quantification of signal was performed using ImageJ software.

494 **Deletion of *Ifih1* in *Smg6*$^{flox/flox}$; *CreERT2* fibroblasts via CRISPR**

495 First, lentiCRISPRv2-Blast-mU6 empty backbone (kind gift from J. Van Leeuwen, Addgene
496 plasmid #206806) [39] was digested with BsmBI (NEB, 0580) enzyme. The digestion products
497 were run on an agarose gel (0.8%), and the band corresponding to the open vector (~11 kb)
498 was excised, followed by DNA purification using QIAquick Gel Extraction Kit. Following
499 annealing reaction was assembled in a tube: 1 µl Forward primer (100 µM), 1 µl Reverse
500 primer (100 µM), 1 µl 10x T4 ligation buffer (NEB, B0202S), 0.5 µl T4 PNK (NEB, B0201S),
501 and 6.5 µl H_2O. Primers were annealed with the following protocol: incubate 30 min at 37°C,

502 and 5 min at 95°C, respectively, then cool to 25°C at a rate of 5°C/min. Annealed primers were
503 ligated into the open vector using the following mixture: 50 ng open vector, 2 µl 10x T4 ligation
504 buffer, 1 µl T4 DNA ligase (NEB, M0202S), 1 µl annealed primers (1:100 diluted), and
505 nuclease-free H_2O to 20 µl. Ligation mix was incubated at RT for 1 h. 10 µl ligation mix was
506 added to 100 µl Stbl3 competent cells, and incubated on ice for 30 min, followed by a heat-
507 shock for 30 sec at 42°C. After a short incubation (5 min, on ice), 1 ml S.O.C. medium was
508 added to the mixture, and the tube was incubated at 37°C, for 1 h with shaking. 100 µl of the
509 transformation mixture was plated on an agar plate containing Ampicillin and incubated
510 overnight at 37°C. Positive colonies were selected and cultured overnight with shaking at
511 37°C, in LB medium containing Ampicillin, then purified using a Midiprep kit (QIAGEN, 12943).
512 Cells were transfected with the plasmid using Lipofectamine 3000 (Thermo Fisher Scientific,
513 L3000001), according to the manufacturer's protocol, for 24 h, then were selected with
514 Blasticidin (5 µg/ml) for 96 h. *Ifih1*$^{ko/ko}$ cells were obtained through single cell cloning. *Ifih1*
515 sgRNA primer sequences: forward, CAC CGC GTA GAC GAC ATA TTA CCA G; reverse,
516 AAA CCT GGT AAT ATG TCG TCT ACG C.

517 **Induction of Cre-mediated recombination in fibroblasts**

518 Two different methods were used to induce Cre-dependent recombination:
519 1-Direct delivery of recombinant CRE protein (TAT-CRE, kind gift from I. Lopez-Mejia)*:*
520 *Smg6*$^{w/wt}$ and *Smg6*$^{flox/flox}$ (-/+ *Ifih1*$^{ko/ko}$) fibroblasts were seeded in 6-well plates. The standard
521 culture medium (Thermo Fisher Scientific, 41965062) was replaced with Opti-MeM (Thermo
522 Fisher Scientific, 31985062). Cells were subsequently treated with 2.5 µM TAT-CRE or vehicle
523 for 8 h. After treatment, OptiMeM was replaced with the standard culture medium.
524 2-Recombination via 4-hydroxytamoxifen (4-OHT): *Smg6*$^{flox/flox}$; *CreERT2* cells were treated
525 with 2 µM 4-OHT or DMSO for 3 days (4-OHT containing media was refreshed every 24 h).
526 In both methods, cells were maintained in culture for at least one-week post-treatment to
527 ensure efficient recombination. Cells were subsequently collected for RNA extraction (as
528 explained above).

529 **J2 immunofluorescence**

530 Immunofluorescence of dsRNA was performed as [40]. First, *Smg6*$^{flox/flox}$ cells were seeded in a
531 6-well plate, then treated with 2.5 µM TAT-CRE or vehicle as above. One week after the
532 treatment, cells were transferred to a new 6-well plate containing coverslips, at a confluency
533 of ca. 20%. Next day, the culture medium was removed, and cells were fixed using 4%
534 paraformaldehyde (PFA) for 15 min at RT, then washed three times (5 min each time), with
535 1x PBS. Fixed cells were permeabilized with 500 µl PBSTX, followed by a 10 min incubation
536 at RT. PBSTX was removed, 500 µl of IFA blocking buffer was added into each well, and

incubated for 1 h, at RT with rocking. After blocking, cells were incubated with 500 µl primary antibody solution (anti-dsRNA monoclonal antibody J2: Jena Bioscience, RNT-SCI-10010200) in IFA blocking buffer (1:1000), overnight, at 4°C with rocking. Primary antibody solution was removed, and cells were washed with 500 µl PBSTX (three times, for 5 min each). Cells were incubated with the secondary antibody solution in PBSTX (1:300, Goat anti-mouse IgG Alexa Fluor 488 for detection of J2, followed by washes with 500 µl PBSTX 3 times, for 5 min each). To prepare the slides for imaging, coverslips were removed from 6-well plate, and cleaned with 70% ethanol, then placed face down onto the glasses, sealed with a nail polish. Images were captured using a fluorescence microscope. The quantification of J2 intensity was performed on ImageJ software.

ACKNOWLEDGEMENTS

We thank the Lausanne Genomic Technologies Facility for library preparation and sequencing, F. Lammers for help with genotyping, C. Roger for histology analysis, G. Niederhäuser for serum measurements, Anne-Claire Godet at www.threoninedesign.fr for the graphical illustration in Figure 4F, I. Lopez-Mejia for providing TAT-CRE, J. Van Leeuwen for providing lentiCRISPRv2-Blast-mU6 plasmid, M. Hall and D. Mossmann for providing L-dKO mice and for scientific inputs, O. Mühlemann and E. Karousis for important discussions. D.G. acknowledges funding by Swiss National Science Foundation (SNSF) NCCR RNA & Disease Phase III funding (grant number 205601), SNSF project grant (212423) and by Novartis Foundation for Medical-Biological Research grant (21B066).

AUTHOR CONTRIBUTIONS

Conceptualization: E.S.A. and D.G.; methodology: E.S.A., V.R., I.E.S., M.J., I.G.-M., and A.P.B.; investigation: E.S.A., V.R., I.E.S., M.J., I.G.-M., and L.Q.-M.; visualization: E.S.A., V.R., I.E.S., M.J., and I.G.-M.; supervision: D.G., L.Q.-M., J.R., S.A.L., and M.B.-S.; writing: E.S.A. and D.G.

DECLARATION OF INTERESTS

The authors declare no competing interests.

DATA AVAILABILITY

The transcriptomics and ribo-seq data discussed in this publication have been deposited in NCBI's Gene Expression Omnibus [41] and are accessible through GEO Series accession numbers GSE278996 and GSE278997. The mass spectrometry proteomics data have been deposited to the ProteomeXchange Consortium via the PRIDE [42] partner repository with the

569 dataset identifier PXD057903. All computational scripts are available on GitHub
570 (https://github.com/NMD_Smg6/).

571 **References**

572 1. Kurosaki, T., Popp, M.W., and Maquat, L.E. (2019). Quality and quantity control of gene
573 expression by nonsense-mediated mRNA decay. Nat Rev Mol Cell Biol *20*, 406-420.
574 10.1038/s41580-019-0126-2.
575 2. Karousis, E.D., and Muhlemann, O. (2022). The broader sense of nonsense. Trends
576 Biochem Sci *47*, 921-935. 10.1016/j.tibs.2022.06.003.
577 3. Lindeboom, R.G.H., Vermeulen, M., Lehner, B., and Supek, F. (2019). The impact of
578 nonsense-mediated mRNA decay on genetic disease, gene editing and cancer
579 immunotherapy. Nat Genet *51*, 1645-1651. 10.1038/s41588-019-0517-5.
580 4. Boehm, V., Kueckelmann, S., Gerbracht, J.V., Kallabis, S., Britto-Borges, T., Altmuller, J.,
581 Kruger, M., Dieterich, C., and Gehring, N.H. (2021). SMG5-SMG7 authorize nonsense-
582 mediated mRNA decay by enabling SMG6 endonucleolytic activity. Nat Commun *12*,
583 3965. 10.1038/s41467-021-24046-3.
584 5. Wu, C.C., Beird, H.C., Andrew Livingston, J., Advani, S., Mitra, A., Cao, S., Reuben, A.,
585 Ingram, D., Wang, W.L., Ju, Z., et al. (2020). Immuno-genomic landscape of
586 osteosarcoma. Nat Commun *11*, 1008. 10.1038/s41467-020-14646-w.
587 6. Litchfield, K., Reading, J.L., Lim, E.L., Xu, H., Liu, P., Al-Bakir, M., Wong, Y.N.S., Rowan,
588 A., Funt, S.A., Merghoub, T., et al. (2020). Escape from nonsense-mediated decay
589 associates with anti-tumor immunogenicity. Nat Commun *11*, 3800. 10.1038/s41467-
590 020-17526-5.
591 7. Oka, M., Xu, L., Suzuki, T., Yoshikawa, T., Sakamoto, H., Uemura, H., Yoshizawa, A.C.,
592 Suzuki, Y., Nakatsura, T., Ishihama, Y., et al. (2021). Aberrant splicing isoforms detected
593 by full-length transcriptome sequencing as transcripts of potential neoantigens in non-
594 small cell lung cancer. Genome Biol *22*, 9. 10.1186/s13059-020-02240-8.
595 8. Zhang, Y., Xie, X., Yeganeh, P.N., Lee, D.J., Valle-Garcia, D., Meza-Sosa, K.F., Junqueira,
596 C., Su, J., Luo, H.R., Hide, W., and Lieberman, J. (2021). Immunotherapy for breast
597 cancer using EpCAM aptamer tumor-targeted gene knockdown. Proc Natl Acad Sci U S
598 A *118*. 10.1073/pnas.2022830118.
599 9. Pastor, F., Kolonias, D., Giangrande, P.H., and Gilboa, E. (2010). Induction of tumour
600 immunity by targeted inhibition of nonsense-mediated mRNA decay. Nature *465*, 227-
601 230. 10.1038/nature08999.
602 10. Meraviglia-Crivelli, D., Villanueva, H., Zheleva, A., Villalba-Esparza, M., Moreno, B.,
603 Menon, A.P., Calvo, A., Cebollero, J., Barainka, M., de Los Mozos, I.R., et al. (2022). IL-
604 6/STAT3 signaling in tumor cells restricts the expression of frameshift-derived
605 neoantigens by SMG1 induction. Mol Cancer *21*, 211. 10.1186/s12943-022-01679-6.
606 11. Meraviglia-Crivelli, D., Villanueva, H., Menon, A.P., Zheleva, A., Moreno, B., Villalba-
607 Esparza, M., and Pastor, F. (2022). A pan-tumor-siRNA aptamer chimera to block
608 nonsense-mediated mRNA decay inflames and suppresses tumor progression. Mol
609 Ther Nucleic Acids *29*, 413-425. 10.1016/j.omtn.2022.07.017.
610 12. Nasif, S., Colombo, M., Uldry, A.C., Schroder, M.S., de Brot, S., and Muhlemann, O.
611 (2023). Inhibition of nonsense-mediated mRNA decay reduces the tumorigenicity of
612 human fibrosarcoma cells. NAR Cancer *5*, zcad048. 10.1093/narcan/zcad048.

613 13. Hwang, J., and Maquat, L.E. (2011). Nonsense-mediated mRNA decay (NMD) in animal
614 embryogenesis: to die or not to die, that is the question. Curr Opin Genet Dev *21*, 422-
615 430. 10.1016/j.gde.2011.03.008.
616 14. Katsioudi, G., Dreos, R., Arpa, E.S., Gaspari, S., Liechti, A., Sato, M., Gabriel, C.H.,
617 Kramer, A., Brown, S.A., and Gatfield, D. (2023). A conditional Smg6 mutant mouse
618 model reveals circadian clock regulation through the nonsense-mediated mRNA decay
619 pathway. Sci Adv *9*, eade2828. 10.1126/sciadv.ade2828.
620 15. Li, T., Shi, Y., Wang, P., Guachalla, L.M., Sun, B., Joerss, T., Chen, Y.S., Groth, M., Krueger,
621 A., Platzer, M., et al. (2015). Smg6/Est1 licenses embryonic stem cell differentiation via
622 nonsense-mediated mRNA decay. EMBO J *34*, 1630-1647. 10.15252/embj.201489947.
623 16. Snoek, M., van Dinten, L., and van Vugt, H. (1996). A novel gene, G7e, resembling a
624 viral envelope gene, is located at the recombinational hot spot in the class III region of
625 the mouse MHC. Genomics *38*, 5-12. 10.1006/geno.1996.0585.
626 17. Du, N.H., Arpat, A.B., De Matos, M., and Gatfield, D. (2014). MicroRNAs shape circadian
627 hepatic gene expression on a transcriptome-wide scale. Elife *3*, e02510.
628 10.7554/eLife.02510.
629 18. Schoggins, J.W., Wilson, S.J., Panis, M., Murphy, M.Y., Jones, C.T., Bieniasz, P., and Rice,
630 C.M. (2011). A diverse range of gene products are effectors of the type I interferon
631 antiviral response. Nature *472*, 481-485. 10.1038/nature09907.
632 19. Bowling, E.A., Wang, J.H., Gong, F., Wu, W., Neill, N.J., Kim, I.S., Tyagi, S., Orellana, M.,
633 Kurley, S.J., Dominguez-Vidana, R., et al. (2021). Spliceosome-targeted therapies
634 trigger an antiviral immune response in triple-negative breast cancer. Cell *184*, 384-
635 403 e321. 10.1016/j.cell.2020.12.031.
636 20. Zheng, R., Dunlap, M., Bobkov, G.O.M., Gonzalez-Figueroa, C., Patel, K.J., Lyu, J.,
637 Harvey, S.E., Chan, T.W., Quinones-Valdez, G., Choudhury, M., et al. (2024). hnRNPM
638 protects against the dsRNA-mediated interferon response by repressing LINE-
639 associated cryptic splicing. Mol Cell *84*, 2087-2103 e2088.
640 10.1016/j.molcel.2024.05.004.
641 21. Dias Junior, A.G., Sampaio, N.G., and Rehwinkel, J. (2019). A Balancing Act: MDA5 in
642 Antiviral Immunity and Autoinflammation. Trends Microbiol *27*, 75-85.
643 10.1016/j.tim.2018.08.007.
644 22. Schonborn, J., Oberstrass, J., Breyel, E., Tittgen, J., Schumacher, J., and Lukacs, N.
645 (1991). Monoclonal antibodies to double-stranded RNA as probes of RNA structure in
646 crude nucleic acid extracts. Nucleic Acids Res *19*, 2993-3000. 10.1093/nar/19.11.2993.
647 23. Pepin, G., Ferrand, J., Honing, K., Jayasekara, W.S., Cain, J.E., Behlke, M.A., Gough, D.J.,
648 BR, G.W., Hornung, V., and Gantier, M.P. (2016). Cre-dependent DNA recombination
649 activates a STING-dependent innate immune response. Nucleic Acids Res *44*, 5356-
650 5364. 10.1093/nar/gkw405.
651 24. Guri, Y., Colombi, M., Dazert, E., Hindupur, S.K., Roszik, J., Moes, S., Jenoe, P., Heim,
652 M.H., Riezman, I., Riezman, H., and Hall, M.N. (2017). mTORC2 Promotes
653 Tumorigenesis via Lipid Synthesis. Cancer Cell *32*, 807-823 e812.
654 10.1016/j.ccell.2017.11.011.
655 25. Postic, C., and Girard, J. (2008). The role of the lipogenic pathway in the development
656 of hepatic steatosis. Diabetes Metab *34*, 643-648. 10.1016/S1262-3636(08)74599-3.
657 26. Schuler, M., Dierich, A., Chambon, P., and Metzger, D. (2004). Efficient temporally
658 controlled targeted somatic mutagenesis in hepatocytes of the mouse. Genesis *39*,
659 167-172. 10.1002/gene.20039.

660 27. Horie, Y., Suzuki, A., Kataoka, E., Sasaki, T., Hamada, K., Sasaki, J., Mizuno, K., Hasegawa,
661 G., Kishimoto, H., Iizuka, M., et al. (2004). Hepatocyte-specific Pten deficiency results
662 in steatohepatitis and hepatocellular carcinomas. J Clin Invest *113*, 1774-1783.
663 10.1172/JCI20513.
664 28. Kwiatkowski, D.J., Zhang, H., Bandura, J.L., Heiberger, K.M., Glogauer, M., el-
665 Hashemite, N., and Onda, H. (2002). A mouse model of TSC1 reveals sex-dependent
666 lethality from liver hemangiomas, and up-regulation of p70S6 kinase activity in Tsc1
667 null cells. Hum Mol Genet *11*, 525-534. 10.1093/hmg/11.5.525.
668 29. Benechet, A.P., De Simone, G., Di Lucia, P., Cilenti, F., Barbiera, G., Le Bert, N.,
669 Fumagalli, V., Lusito, E., Moalli, F., Bianchessi, V., et al. (2019). Dynamics and genomic
670 landscape of CD8(+) T cells undergoing hepatic priming. Nature *574*, 200-205.
671 10.1038/s41586-019-1620-6.
672 30. Gatfield, D., Le Martelot, G., Vejnar, C.E., Gerlach, D., Schaad, O., Fleury-Olela, F.,
673 Ruskeepaa, A.L., Oresic, M., Esau, C.C., Zdobnov, E.M., and Schibler, U. (2009).
674 Integration of microRNA miR-122 in hepatic circadian gene expression. Genes Dev *23*,
675 1313-1326. 10.1101/gad.1781009.
676 31. Dobin, A., Davis, C.A., Schlesinger, F., Drenkow, J., Zaleski, C., Jha, S., Batut, P., Chaisson,
677 M., and Gingeras, T.R. (2013). STAR: ultrafast universal RNA-seq aligner. Bioinformatics
678 *29*, 15-21. 10.1093/bioinformatics/bts635.
679 32. Love, M.I., Huber, W., and Anders, S. (2014). Moderated estimation of fold change and
680 dispersion for RNA-seq data with DESeq2. Genome Biol *15*, 550. 10.1186/s13059-014-
681 0550-8.
682 33. Snieckute, G., Ryder, L., Vind, A.C., Wu, Z., Arendrup, F.S., Stoneley, M., Chamois, S.,
683 Martinez-Val, A., Leleu, M., Dreos, R., et al. (2023). ROS-induced ribosome impairment
684 underlies ZAKalpha-mediated metabolic decline in obesity and aging. Science *382*,
685 eadf3208. 10.1126/science.adf3208.
686 34. Martin, M. (2011). Cutadapt removes adapter sequences from high-throughput
687 sequencing reads. EMBnet.journal *17*, 10-12.
688 35. Lawrence, M., Huber, W., Pages, H., Aboyoun, P., Carlson, M., Gentleman, R., Morgan,
689 M.T., and Carey, V.J. (2013). Software for computing and annotating genomic ranges.
690 PLoS Comput Biol *9*, e1003118. 10.1371/journal.pcbi.1003118.
691 36. Chong, C., Marino, F., Pak, H., Racle, J., Daniel, R.T., Muller, M., Gfeller, D., Coukos, G.,
692 and Bassani-Sternberg, M. (2018). High-throughput and Sensitive
693 Immunopeptidomics Platform Reveals Profound Interferongamma-Mediated
694 Remodeling of the Human Leukocyte Antigen (HLA) Ligandome. Mol Cell Proteomics
695 *17*, 533-548. 10.1074/mcp.TIR117.000383.
696 37. Kong, A.T., Leprevost, F.V., Avtonomov, D.M., Mellacheruvu, D., and Nesvizhskii, A.I.
697 (2017). MSFragger: ultrafast and comprehensive peptide identification in mass
698 spectrometry-based proteomics. Nat Methods *14*, 513-520. 10.1038/nmeth.4256.
699 38. Gfeller, D., Schmidt, J., Croce, G., Guillaume, P., Bobisse, S., Genolet, R., Queiroz, L.,
700 Cesbron, J., Racle, J., and Harari, A. (2023). Improved predictions of antigen
701 presentation and TCR recognition with MixMHCpred2.2 and PRIME2.0 reveal potent
702 SARS-CoV-2 CD8(+) T-cell epitopes. Cell Syst *14*, 72-83 e75. 10.1016/j.cels.2022.12.002.
703 39. Unlu, B., Pons, C., Ho, U.L., Batte, A., Aloy, P., and van Leeuwen, J. (2023). Global
704 analysis of suppressor mutations that rescue human genetic defects. Genome Med *15*,
705 78. 10.1186/s13073-023-01232-0.

706 40. de Faria, I.J.S., Imler, J.L., and Marques, J.T. (2023). Protocol for the analysis of double-
707 stranded RNAs in virus-infected insect cells using anti-dsRNA antibodies. STAR Protoc
708 *4*, 102033. 10.1016/j.xpro.2022.102033.
709 41. Edgar, R., Domrachev, M., and Lash, A.E. (2002). Gene Expression Omnibus: NCBI gene
710 expression and hybridization array data repository. Nucleic Acids Res *30*, 207-210.
711 10.1093/nar/30.1.207.
712 42. Perez-Riverol, Y., Bai, J., Bandla, C., Garcia-Seisdedos, D., Hewapathirana, S.,
713 Kamatchinathan, S., Kundu, D.J., Prakash, A., Frericks-Zipper, A., Eisenacher, M., et al.
714 (2022). The PRIDE database resources in 2022: a hub for mass spectrometry-based
715 proteomics evidences. Nucleic Acids Res *50*, D543-D552. 10.1093/nar/gkab1038.

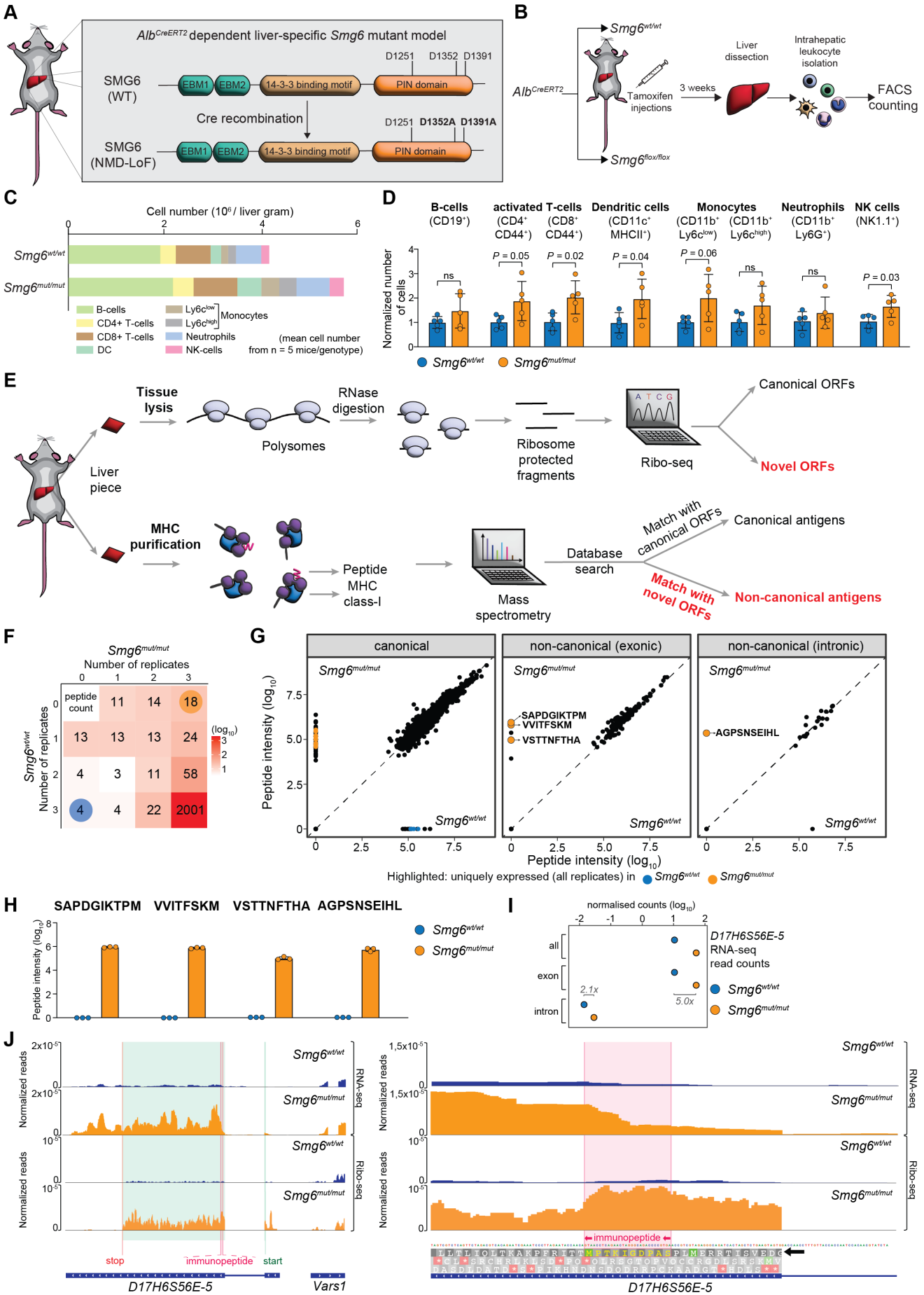
A
Alb^CreERT2 dependent liver-specific Smg6 mutant model
SMG6 (WT)
EBM1
EBM2
14-3-3 binding motif
PIN domain
D1251
D1352
D1391
Cre recombination
SMG6 (NMD-LoF)
D1251
D1352A
D1391A
B
Smg6^wt/wt
Alb^CreERT2
Tamoxifen injections
3 weeks
Liver dissection
Intrahepatic leukocyte isolation
FACS counting
Smg6^flox/flox
C
Cell number (10^6 / liver gram)
Smg6^wt/wt
Smg6^mut/mut
B-cells
CD4+ T-cells
CD8+ T-cells
DC
Ly6c^low
Ly6c^high
Monocytes
Neutrophils
NK-cells
(mean cell number from n = 5 mice/genotype)
D
B-cells (CD19+)
activated T-cells (CD4+ CD44+) (CD8+ CD44+)
Dendritic cells (CD11c+ MHCII+)
Monocytes (CD11b+ Ly6c^low) (CD11b+ Ly6c^high)
Neutrophils (CD11b+ Ly6G+)
NK cells (NK1.1+)
Normalized number of cells
ns
P = 0.05
P = 0.02
P = 0.04
P = 0.06
ns
ns
P = 0.03
Smg6^wt/wt
Smg6^mut/mut
E
Tissue lysis
Liver piece
Polysomes
RNase digestion
Ribosome protected fragments
Ribo-seq
Canonical ORFs
Novel ORFs
MHC purification
Peptide MHC class-I
Mass spectrometry
Database search
Match with canonical ORFs
Match with novel ORFs
Canonical antigens
Non-canonical antigens
F
Smg6^mut/mut
Number of replicates
Smg6^wt/wt
Number of replicates
peptide count
11
14
18
13
13
13
24
4
3
11
58
4
4
22
2001
(log10)
G
canonical
non-canonical (exonic)
non-canonical (intronic)
Smg6^mut/mut
Smg6^wt/wt
Peptide intensity (log10)
SAPDGIKTPM
VVITFSKM
VSTTNFTHA
AGPSNSEIHL
Highlighted: uniquely expressed (all replicates) in Smg6^wt/wt Smg6^mut/mut
H
SAPDGIKTPM
VVITFSKM
VSTTNFTHA
AGPSNSEIHL
Peptide intensity (log10)
Smg6^wt/wt
Smg6^mut/mut
I
normalised counts (log10)
all
exon
intron
2.1x
5.0x
D17H6S56E-5 RNA-seq read counts
Smg6^wt/wt
Smg6^mut/mut
J
Normalized reads
RNA-seq
Ribo-seq
Smg6^wt/wt
Smg6^mut/mut
stop
immunopeptide
start
D17H6S56E-5
Vars1
immunopeptide
D17H6S56E-5

716 **Figure 1. Increased non-canonical immunopeptide expression in *Smg6* mutant livers**

717 (A) Schematic of the genetic NMD-deficient mouse model. Cre-mediated recombination
718 of the *Smg6*^{flox} allele to *Smg6*^{mut} introduces two-point mutations in catalytically
719 important residues of the PIN domain. EBM, exon-junction complex binding motif.
720 LoF, loss of function.

721 (B) Schematic of the experimental design for intrahepatic leukocyte isolation and flow
722 cytometry-based counting. *Smg6*$^{wt/wt}$ and *Smg6*$^{flox/flox}$ mice (both also expressing
723 *Alb*^{CreERT2}) received 4 intraperitoneal tamoxifen injections. Livers were dissected 3
724 weeks later, and leukocytes were isolated for flow cytometric quantification. FACS,
725 fluorescence-associated cell sorting.

726 (C) Overall leukocyte numbers per gram liver tissue (mean values from 5 mice per group),
727 as assessed by flow cytometry. Cells are identified according to indicated color code.

728 (D) Relative leukocyte counts for individual cell types as assessed by flow cytometry.
729 Graphs show normalized numbers (set to 1 in control) of indicated leukocyte type (n
730 = 5 mice for each group. Data are plotted as means, and the error bars indicate SEM.
731 The *P*-values were calculated with two-tailed unpaired *t*-test. DC, dendritic cells; NK,
732 natural killer; ns, not significant.

733 (E) Schematic of the immunopeptide identification by combining ribo-seq and
734 immunopeptidomics data.

735 (F) MHC-I binder peptide count and distribution across *Smg6*$^{wt/wt}$ and *Smg6*$^{mut/mut}$ liver
736 replicates (n = 3 mice per genotype). Enrichment of unique peptides in *Smg6*$^{mut/mut}$
737 samples (18 in all replicates) as compared to *Smg6*$^{wt/wt}$ (4 in all replicates) is highly
738 significant (P = 0.000053; Fisher's exact test).

739 (G) Scatter plots show canonical and non-canonical (exonic or intronic) peptide intensity
740 in *Smg6*$^{wt/wt}$ (x-axis) and *Smg6*$^{mut/mut}$ (y-axis). Data are plotted as medians from the
741 three replicates. Unique peptides in all three replicates are colored orange (mutant-
742 specific peptides) and blue (control-specific peptides), with specific peptides
743 highlighted and annotated with their sequence.

744 (H) Bar plot of peptide intensity of *Smg6* mutant-specific non-canonical antigens (n = 3
745 mice for each group).

746 (I) Normalized exonic and intronic RNA-seq read counts of *D17H6S56E-5*. Each dot
747 represents the merged sequencing data from three biological replicates/livers.

748 (J) RNA-seq (top-panels) and ribo-seq (bottom-panels) read pileup plots show the
749 upregulated transcript and footprint abundance of *D17H6S56E-5* in *Smg6*$^{mut/mut}$. Left
750 panel shows the larger genomic region, including the CDS (highlighted in turquoise)
751 from which the non-canonical polypeptide is translated, while the right panel zooms
752 in the specific region where the immunopeptide is translated (highlighted in light-

753 magenta). Plots were generated using merged sequencing data from three biological
754 replicates (individual livers) per group. Please note gene orientation from right to left.

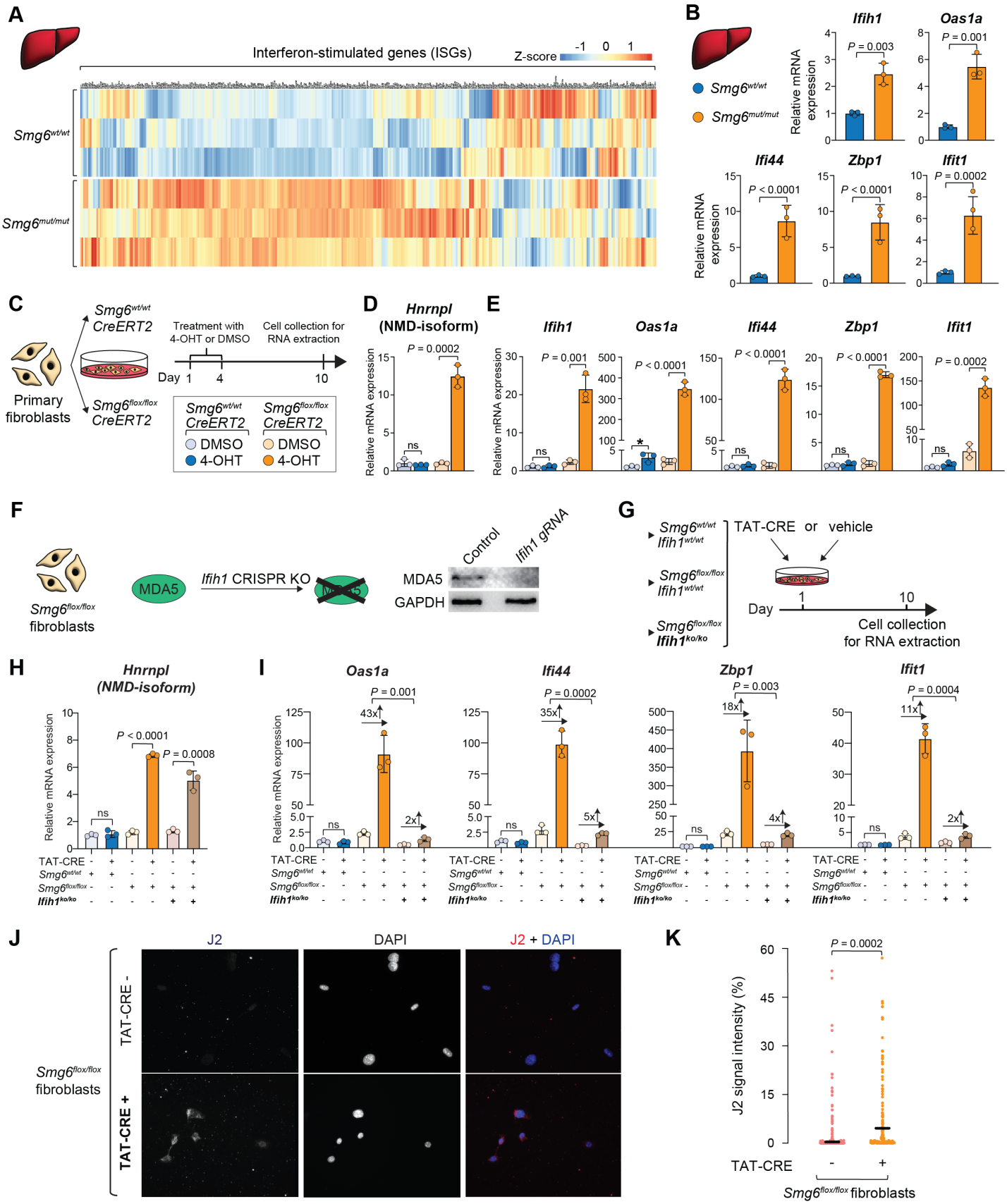
A
Interferon-stimulated genes (ISGs)
Z-score
-1 0 1
Smg6wt/wt
Smg6mut/mut
B
Smg6wt/wt
Smg6mut/mut
Relative mRNA expression
Ifih1
Oas1a
Ifi44
Zbp1
Ifit1
P = 0.003
P = 0.001
P < 0.0001
P = 0.0002
C
Primary fibroblasts
Smg6wt/wt CreERT2
Smg6flox/flox CreERT2
Treatment with 4-OHT or DMSO
Cell collection for RNA extraction
Day 1 4 10
DMSO
4-OHT
D
Hnrnpl (NMD-isoform)
E
F
Smg6flox/flox fibroblasts
MDA5
Ifih1 CRISPR KO
Control
Ifih1 gRNA
GAPDH
G
Smg6wt/wt Ifih1wt/wt
Smg6flox/flox Ifih1wt/wt
Smg6flox/flox Ifih1ko/ko
TAT-CRE or vehicle
Day 1 10
Cell collection for RNA extraction
H
I
P < 0.0001
P = 0.0008
P = 0.0002
P = 0.0004
43x
35x
18x
11x
2x
5x
4x
TAT-CRE
Smg6wt/wt
Smg6flox/flox
Ifih1ko/ko
J
J2
DAPI
J2 + DAPI
TAT-CRE -
TAT-CRE +
Smg6flox/flox fibroblasts
K
J2 signal intensity (%)
TAT-CRE
Smg6flox/flox fibroblasts

755 **Figure 2. *Smg6* mutation results in a Type-I IFN response mediated by dsRNA sensor**
756 **MDA5.**

757 (A) Heatmap showing ISG expression in control and mutant livers (n = 3 livers for each
758 group). RNA-seq data was plotted after Z-score transformation of normalized
759 expression levels across the 6 samples.

760 (B) Relative hepatic mRNA levels of indicated ISGs (n = 3 mice for each group). Control
761 samples were set to 1.

762 (C) Schematic of the experiment to analyze SMG6-dependent ISG expression. To induce
763 *Smg6* mutation in *Smg6*$^{flox/flox}$; *CreERT2* fibroblasts, cells were treated with 2 μM 4-
764 hydroxytamoxifen (4-OHT) during days 1 to 4, and cells were collected 6 days later
765 (day 10) for RNA isolation and qPCR. Control treatment was DMSO.

766 (D) Relative mRNA expression of the endogenous, diagnostic NMD-target, an *Hnrnpl*
767 splice form, in samples collected as described in (C). Three biological replicates were
768 used per group.

769 (E) Relative mRNA expression of indicated ISGs in same samples as in (D). Three
770 biological replicates were used per group.

771 (F) Western blot validation of the loss of MDA5 expression in *Ifih1*$^{ko/ko}$ fibroblasts
772 (*Smg6*$^{flox/flox}$ cells). GAPDH serves as loading control.

773 (G) Schematic of the experiment. Cells with indicated genotypes were treated with either
774 TAT-CRE (2.5 μM) or vehicle for 8 hours, and then harvested at day 10 for RNA
775 extraction and qPCR analyses.

776 (H) Relative mRNA expression of the endogenous, diagnostic NMD-target, an *Hnrnpl*
777 splice form, in samples collected as described in (G). Three biological replicates were
778 used per group.

779 (I) Relative mRNA expression of indicated ISGs. Arrows indicate the fold-change in the
780 expression of indicated genes between cells nontreated vs. treated with TAT-CRE.
781 Three biological replicates were used per group.

782 (J) Representative images from J2 (red) immunofluorescence (IF). DAPI (blue) serves to
783 visualize nuclei.

784 (K) Quantification of J2 signal intensity (n = 238 cells for TAT-CRE-negative, n = 185 cells
785 for TAT-CRE-positive). Black lines indicate the third quartile of each group.

786 For (B), (D), (E), (H), (I), and (K) data are plotted as means, and the error bars indicate
787 SEM. The *P*-values were calculated with two-tailed unpaired *t*-test.

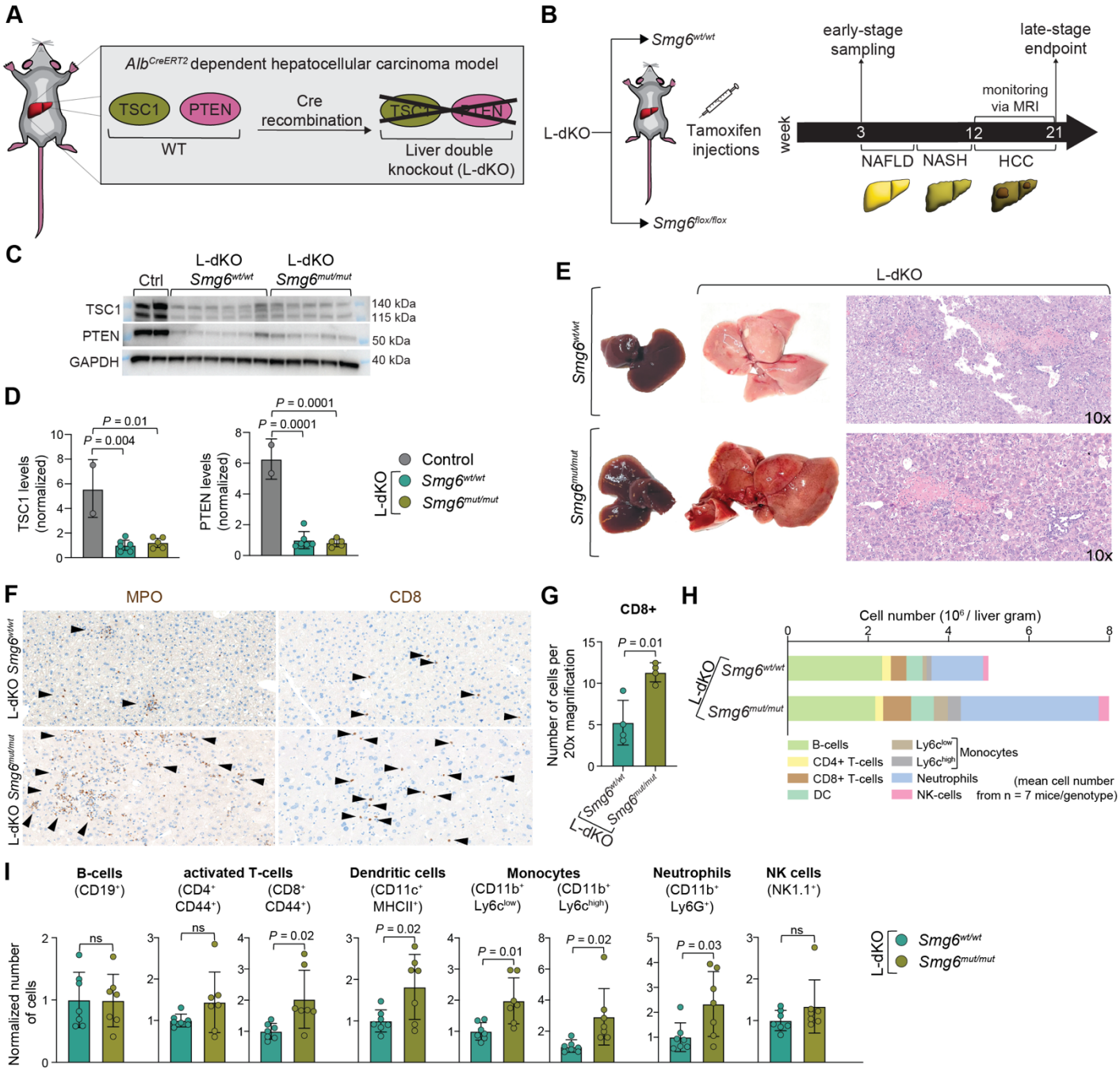

Figure 3. SMG6-dependent early inflammation in early-stage hepatocellular carcinoma model.

(A) Schematic of the genetic HCC model. Inactivation of tumor suppressor genes *Tsc1* and *Pten* via Cre-mediated recombination leads to tumors/HCC from week 12.

(B) Schematic of the experimental design. Both L-dKO *Smg6*$^{wt/wt}$ and *Smg6*$^{flox/flox}$ mice received 4 intraperitoneal tamoxifen injections. Early-stage experiment was terminated 3 weeks after tamoxifen injections. Late-stage animals were scanned via MRI from

795 week 12 to 21 (endpoint). In L-dKO *Smg6*$^{wt/wt}$, livers undergo NAFLD and NASH stages
796 as indicated.
797 (C) Western blot analysis on total liver proteins, for PTEN and TSC1. GAPDH serves as
798 loading control (Control, n = 2 mice; L-dKO *Smg6*^{wt}, n = 6 mice; L-dKO *Smg6*^{mut}, n = 5
799 mice).
800 (D) Quantification of western blots from (C).
801 (E) Representative images of whole-livers and Hematoxylin and Eosin (H&E)-stained
802 sections (at 10x magnification) from early-stage L-dKO *Smg6*^{wt} and *Smg6*^{mut} mice.
803 (F) Representative IHC images of livers from early-stage mice against neutrophil marker
804 Myeloperoxidase (MPO) and T-cell marker CD8, at 20x magnification. Arrowheads
805 mark MPO-positive or CD8-positive cells (brown).
806 (G) Quantification of CD8 IHC images. For each sample, the number of CD8+ T-cells was
807 counted in 15 randomly selected images, at 20x magnification (mean values from 4
808 mice per group).
809 (H) Overall leukocyte numbers per gram liver tissue (mean values from 7 mice per group),
810 as assessed by flow cytometry. Cells are identified according to indicated color code.
811 (I) Relative leukocyte counts for individual cell types as assessed by flow cytometry.
812 Graphs show normalized numbers (set to 1 in control) of indicated leukocyte type (n =
813 7 mice for each group).
814 For (D), (G), and (I) data are plotted as means, and the error bars indicate SEM. The *P*-
815 values were calculated with two-tailed unpaired *t*-test.

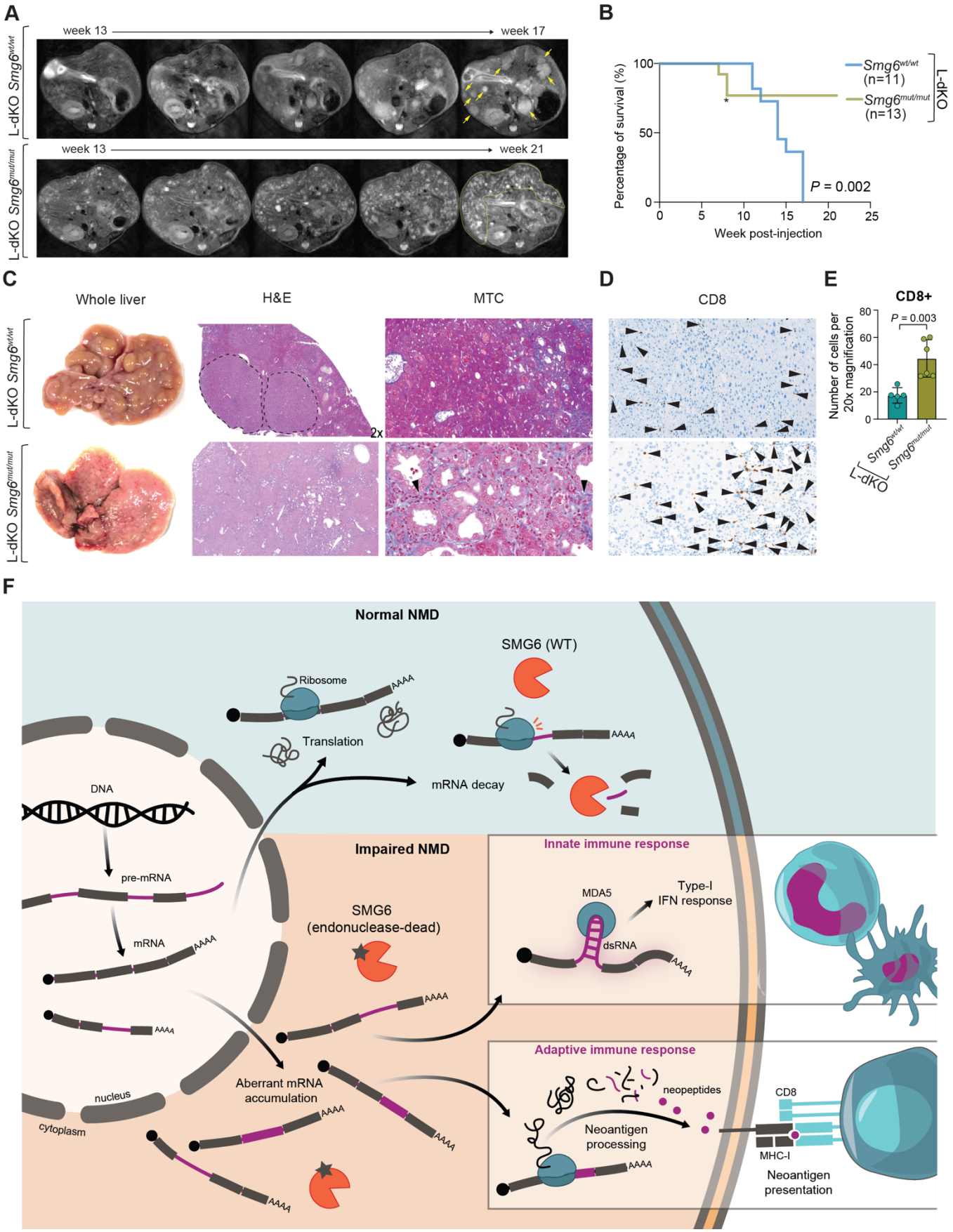
A
week 13
week 17
L-dKO Smg6wt/wt
week 13
week 21
L-dKO Smg6mut/mut
B
Percentage of survival (%)
100
50
0
0
5
10
15
20
25
Week post-injection
Smg6wt/wt (n=11)
Smg6mut/mut (n=13)
L-dKO
P = 0.002
C
Whole liver
H&E
MTC
L-dKO Smg6wt/wt
L-dKO Smg6mut/mut
2x
D
CD8
E
CD8+
Number of cells per 20x magnification
80
60
40
20
0
P = 0.003
Smg6wt/wt
Smg6mut/mut
L-dKO
F
Normal NMD
SMG6 (WT)
Ribosome
AAAA
Translation
mRNA decay
DNA
pre-mRNA
mRNA
Impaired NMD
SMG6 (endonuclease-dead)
Aberrant mRNA accumulation
nucleus
cytoplasm
Innate immune response
MDA5
Type-I IFN response
dsRNA
Adaptive immune response
neopeptides
Neoantigen processing
CD8
MHC-I
Neoantigen presentation

816 **Figure 4. *Smg6* mutation suppresses cancer in genetic HCC model.**

817 (A) Representative longitudinal MRI scans for a tumor-bearing L-dKO *Smg6*^{wt} mouse (top)
818 and a tumor-free L-dKO *Smg6*^{mut} animal. Tumors in L-dKO *Smg6*^{wt} liver are indicated
819 with yellow arrows (upper). Fibrotic plaques marked by yellow line in L-dKO *Smg6*^{mut}
820 liver (lower).

821 (B) Kaplan-Meier plot, from two different cohorts, displays survival percentage of L-dKO
822 *Smg6*^{wt} (n = 11) and *Smg6*^{mut} (n = 13) mice throughout the experiment. *P*-value by a
823 log-rank (Mantel-Cox) test. Asterisk indicates 3 animals that deceased for other
824 reasons than HCC.

825 (C) Whole liver, Masson's Trichrome (MTC) staining for fibrosis (at 20x magnification) and
826 H&E images (at 2x magnification) from late-stage L-dKO *Smg6*^{wt} and *Smg6*^{mut} mice.
827 Dashed lines surround tumors in L-dKO *Smg6*^{wt}. Arrowheads indicate fibrotic areas in
828 L-dKO *Smg6*^{mut}.

829 (D) Representative IHC images of livers from late-stage mice, showing CD8-positive cells,
830 at 20x magnification. Arrowheads mark CD8+ T-cells (brown).

831 (E) Quantification of CD8 IHC images. For each sample, the number of CD8-positive T-
832 cells was counted in 15 randomly selected images, at 20x magnification (L-dKO
833 *Smg6*^{wt}, n = 5 mice; L-dKO *Smg6*^{mut}, n = 6 mice). The *P*-value was calculated with two-
834 tailed unpaired *t*-test.

835 (F) Model for how the suppression of NMD activity via endonuclease-inactive SMG6
836 activates both innate and adaptive branches of the immune system. For innate
837 responses, aberrant mRNAs (shown here: intron-retained transcripts known to contain
838 repetitive elements) can form double-stranded configurations, causing activation of
839 cytoplasmic dsRNA sensor MDA5, which upregulates a type-I IFN response, resulting
840 in innate immune cell infiltration. With the accumulation of aberrant or otherwise NMD-
841 suppressed mRNAs in the cytoplasm, their translation leads to the production of
842 unusual/non-canonical peptides which are then subsequently processed for MHC-I
843 presentation on the cell surface, which attracts CD8+ T-cells to infiltrate the tissue,
844 leading to adaptive immune cell recognition. Please note that for simplicity, prior steps
845 required for CD8+ T-cell activation (i.e., antigen presentation by dendritic cells) have
846 been omitted from the schematic.

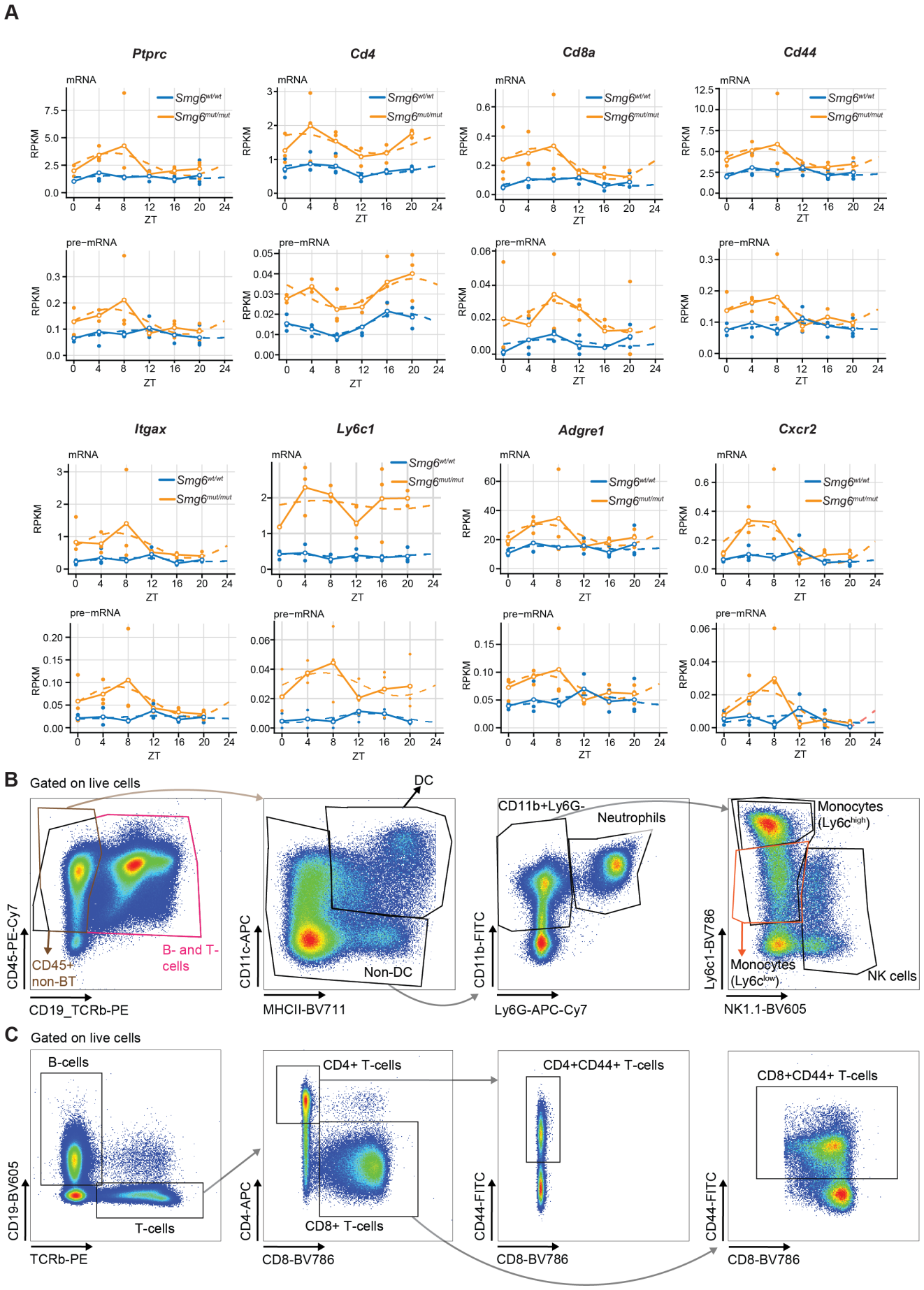
A
Ptprc
Cd4
Cd8a
Cd44
Itgax
Ly6c1
Adgre1
Cxcr2
mRNA
pre-mRNA
RPKM
ZT
Smg6wt/wt
Smg6mut/mut
B
Gated on live cells
CD45-PE-Cy7
CD19_TCRb-PE
CD45+ non-BT
B- and T-cells
DC
CD11c-APC
MHCII-BV711
Non-DC
CD11b+Ly6G-
Neutrophils
CD11b-FITC
Ly6G-APC-Cy7
Monocytes (Ly6chigh)
Monocytes (Ly6clow)
NK cells
Ly6c1-BV786
NK1.1-BV605
C
Gated on live cells
B-cells
T-cells
CD19-BV605
TCRb-PE
CD4+ T-cells
CD8+ T-cells
CD4-APC
CD8-BV786
CD4+CD44+ T-cells
CD44-FITC
CD8+CD44+ T-cells

847 **Figure S1. *Smg6* mutation leads to leukocyte infiltration in the liver.**

848 (A) Hepatic transcriptomics data are plotted for indicated leukocyte-marker genes for
849 mRNA (top graphs) and pre-mRNA (bottom graphs), for *Smg6wt* and *Smg6mut* liver
850 (n = 3 mice per group, for every time-point). RPKM values (reads per kilobase of
851 transcript per million mapped reads) of individual mouse livers are displayed as dots
852 with lines connecting the means for every time point. The dashed lines show the
853 rhythmic data fit using the parameters from Metacycle 41.Samples were taken every
854 4 hours, over a 24-hour period, from light- dark 12:12 entrained mice. ZT: Zeitgeber
855 Time. *Ptprc* (encoding CD45), global leukocyte marker; *Cd4*, CD4+ T-cell marker;
856 *Cd8a*, CD8+ T-cell marker; *Cd44*, activated T-cell marker; *Itgax* (encoding CD11c), DC
857 marker; *Ly6c1* (encoding Ly6c), monocyte marker; *Adgre1* (encoding F4/80),
858 macrophage marker; and *Cxcr2*, neutrophil marker.

859 (B) Flow cytometry gating strategy of intrahepatic myeloid cells.

860 (C) Flow cytometry gating strategy of intrahepatic lymphocytes.

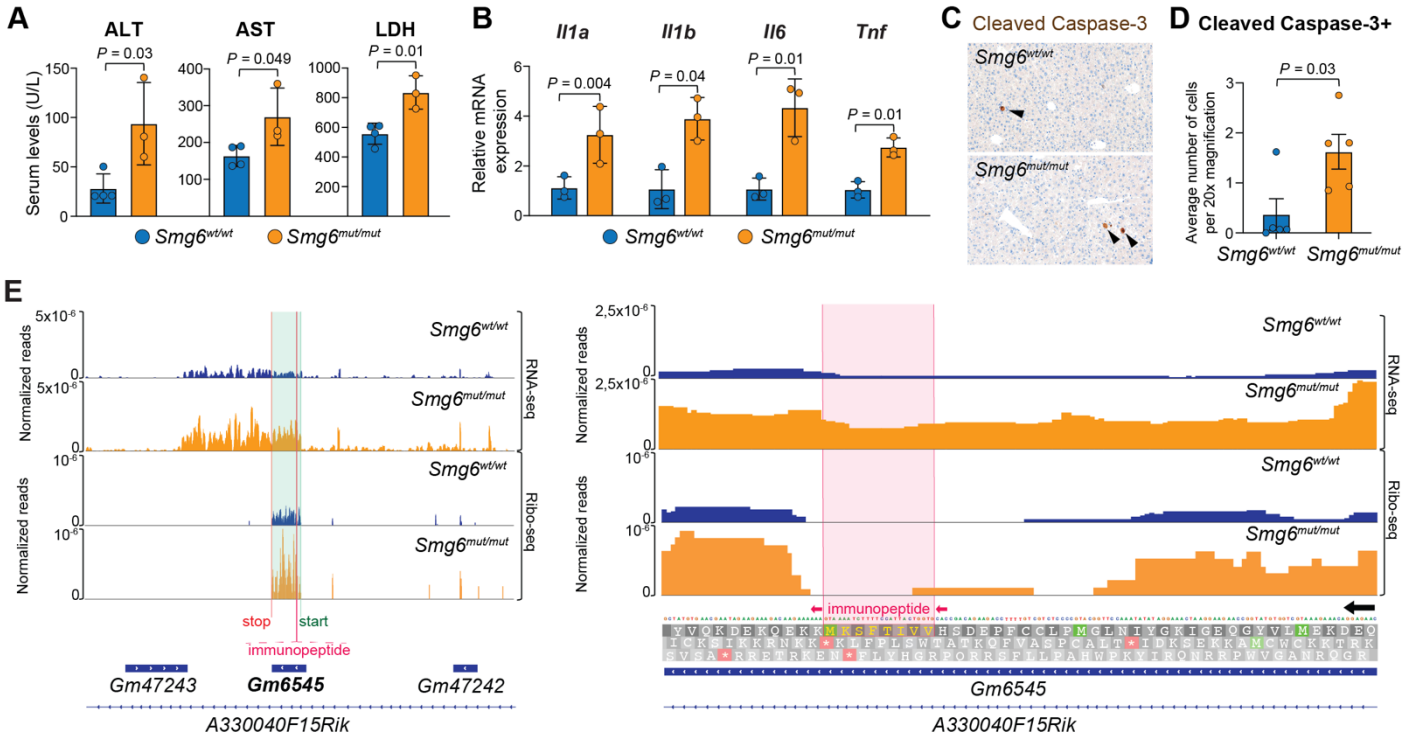

Figure S2. Increased non-canonical antigen expression in *Smg6* mutant livers

(A) Serum levels (U/L) of indicated liver damage markers ($Smg6^{wt}$, n = 4 mice; $Smg6^{wt}$, n = 3 mice).

(B) Relative mRNA levels of indicated inflammatory genes in wild-type vs. mutant livers (n = 3 mice for each group).

(C) Representative IHC images of lviers stained for cleaved Caspase-3 (brown staining), at 20x magnification. Arrowheads show positively stained cells.

(D) Quantification of cleaved Caspase-3 IHC images. For each sample, the number of cleaved Caspase-3 positive cells were counted in 10 randomly selected images, at 20x magnification (mean values from 4 mice per group).

(E) RNA-seq (top-panels) and ribo-seq (bottom-panels) read coverage plots show upregulated transcript and ribosome footprint abundance of *Gm6545* in $Smg6^{mut/mut}$ compared to $Smg6^{wt/wt}$. Left panel shows the whole genomic region, including the CDS (highlighted in turquoise) where the non-canonical polypeptide is translated, while right panel zooms into the specific region where the immunopeptide is translated (highlighted in light-magenta). Read coverage plots were generated by merging sequencing data from three biological replicates (individual livers) per group.

For (A), (B), and (D) data are plotted as means, and the error bars indicate SEM. The *P*-values were calculated with two-tailed unpaired *t*-test.

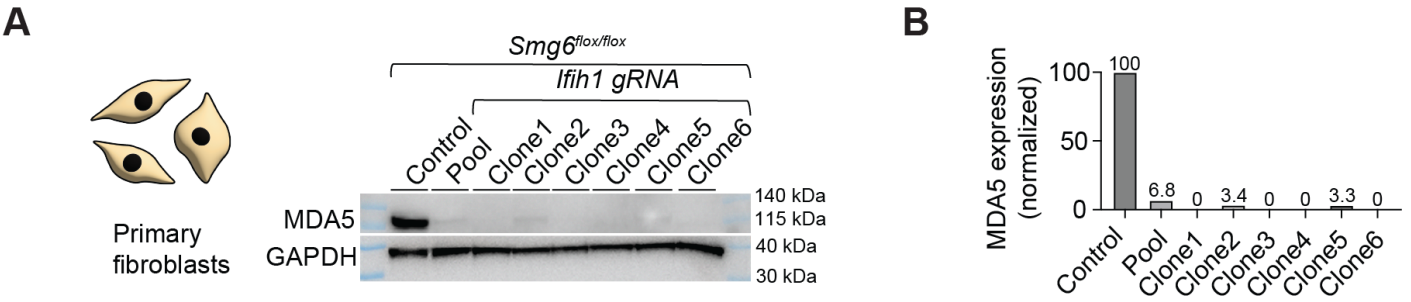

Figure S3. Deletion of *Ifih1* in *Smg6*$^{flox/flox}$ fibroblasts via CRISPR.

(A) Western blot confirmation of the loss of MDA5 activity in different fibroblast single-cell clones. GAPDH serves as loading control.

(B) Quantification of western blot from (A).

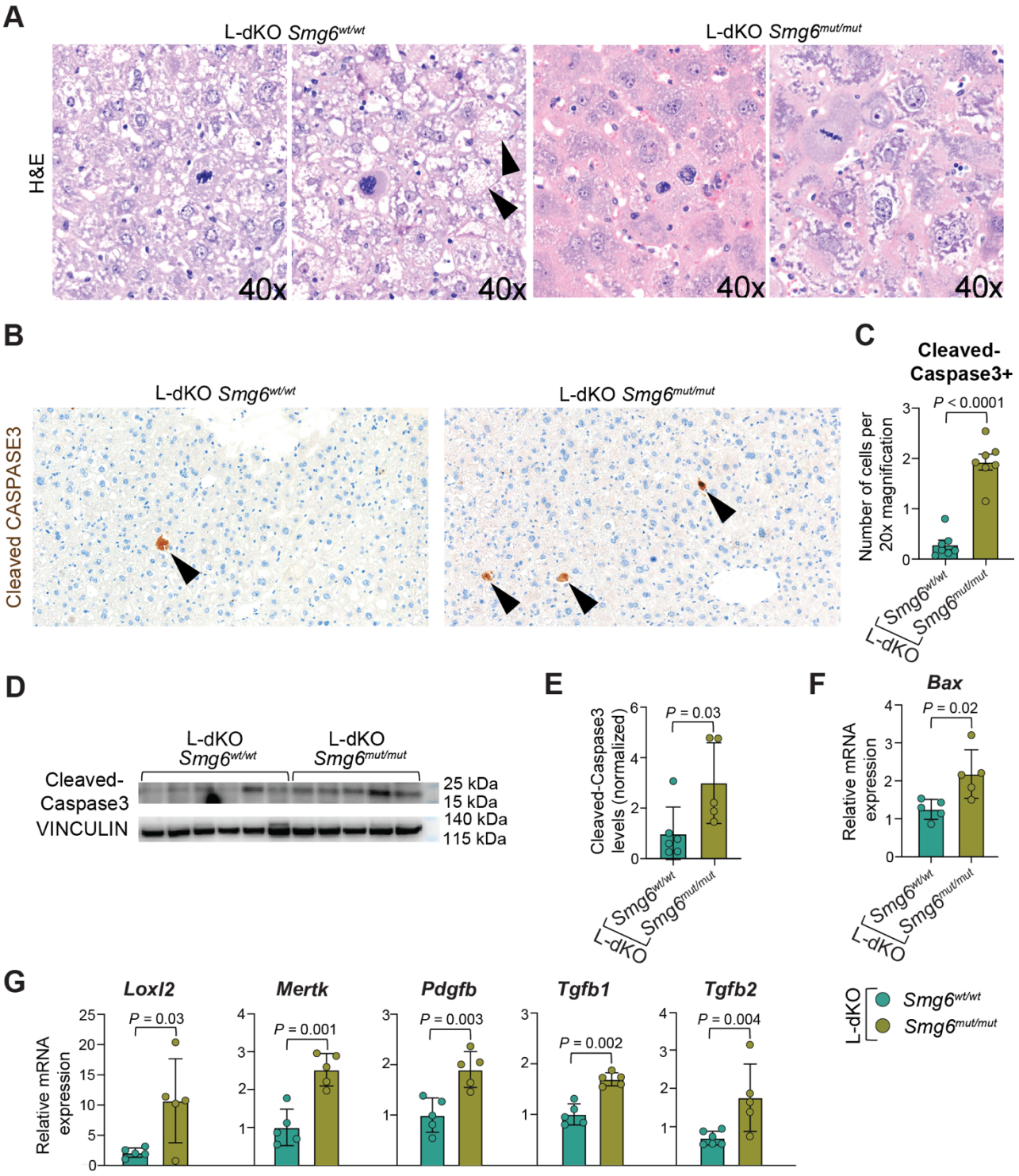

Figure S4. *Smg6* mutation in liver leads to increased apoptosis, followed by fibrosis.

(A) Representative H&E images from early-stage L-dKO livers, at 40x magnification. Arrowheads indicate lipid droplets (white circles) within hepatocytes.

(B) Representative IHC images of livers from early-stage mice, stained with antibodies directed against cleaved Caspase-3, at 20x magnification. Arrowheads show cleaved Caspase-3+ cells (brown).

890 (C) Quantification of cleaved Caspase-3 IHC images as that shown in (B). For each
891 sample, the number of cleaved Caspase-3+ cells was counted in 10 randomly selected
892 images, at 20x magnification (mean values from 7 mice per group).
893 (D) Western blot analysis of total proteins, for cleaved Caspase-3. VINCULIN served as
894 loading control (L-dKO *Smg6*^{wt}, n = 6 mice; L-dKO *Smg6*^{mut}, n = 5 mice).
895 (E) Quantification of western blot from (D).
896 (F) Relative hepatic mRNA levels of *Bax*, from early-stage mice (n = 5 mice per group).
897 (G) Relative hepatic mRNA levels of indicated pro-fibrotic genes, from early-stage mice (n
898 = 4 mice per group).
899 For (C), (E), (F), and (G) data are plotted as means, and the error bars indicate SEM. The
900 *P*-values were calculated with two-tailed unpaired *t*-test.

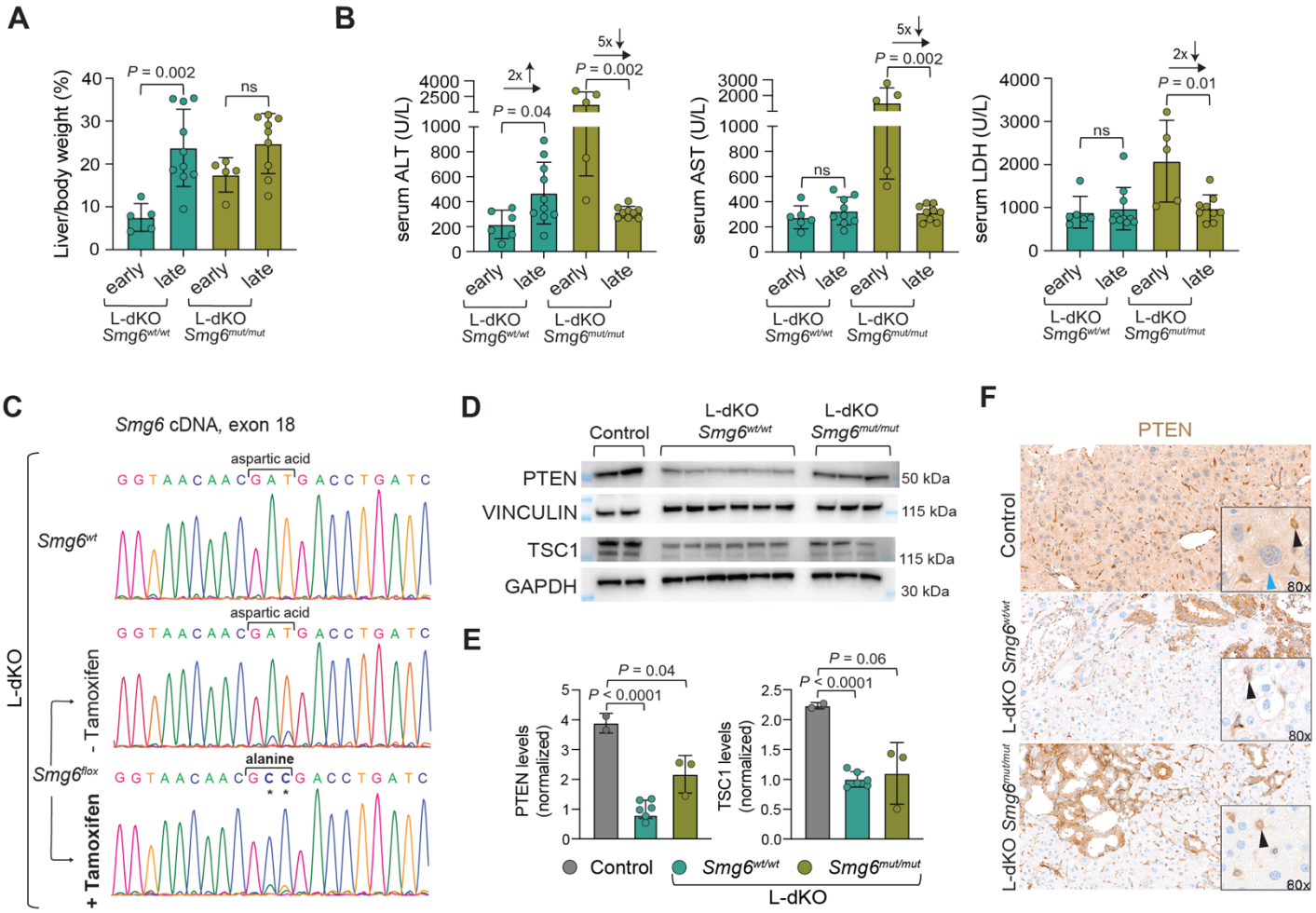

Figure S5. Regression of liver damage marker levels in *Smg6* mutant mice from early- to late-stage L-dKO.

(A) Comparison of the ration of liver-over-body weight between early- and late-stage mice, within the same group (n = 5 mice for early-stage groups; L-dKO *Smg6*^{wt} late, n = 10 mice; L-dKO *Smg6*^{mut} late, n = 9 mice).

(B) Comparison of the level of indicated liver damage enzymes, detected in serum, between early- and late-stage mice. Arrows display the fold-change alteration in the level of liver damage markers from early-to late-stage, in the same group (n = 5 mice for early-stage groups; L-dKO *Smg6*^{wt} late, n = 10 mice; L-dKO *Smg6*^{mut} late, n = 9 mice).

(C) Sanger sequencing chromatograms on cDNA, from representative late-stage livers, show the conversion of aspartic acid encoding wild-type codon (GAC) to alanine encoding mutant codon (GCC) in the exon 18 of the *Smg6* gene, through tamoxifen induced CreERT2 expression in liver.

915 (D) Western blot analysis of total liver proteins for PTEN and TSC1. VINCULIN and
916 GAPDH served as loading controls (Control, n = 2 mice; L-dKO *Smg6*^{wt}, n = 6 mice; L-
917 dKO *Smg6*^{mut}, n = 3 mice).
918 (E) Quantification of western blots from (D).
919 (F) Representative IHC images of livers from late-stage mice against PTEN. Light brown
920 staining shows PTEN expression in hepatocytes in control (blue arrowhead). Dark
921 brown staining indicated PTEN expression in non-hepatocyte cells in both control and
922 L-dKO (black arrowhead). Images were captured at 20x (large images) and 80x (small
923 images) magnifications.
924 For (A), (B), and (E) data are plotted as means, and the error bars indicate SEM. The *P*-
925 values were calculated with two-tailed unpaired *t*-test.